Open Research Online

The Open University's repository of research publications
and other research outputs

Observing the variation of asteroid thermal inertia with heliocentric distance

Journal Item

oro.open.ac.uk

Observing the variation of asteroid thermal inertia with heliocentric distance

B. Rozitis[a], S. F. Green[a], E. MacLennan[b] & J. P. Emery[b]

[a]Planetary and Space Sciences, School of Physical Sciences, The Open University, Walton Hall, Milton Keynes, MK7 6AA, UK

[b]Department of Earth and Planetary Sciences, University of Tennessee, Knoxville, Tennessee 37996, USA

No. of Manuscript Pages: 48
No. of Figures: 12
No. of Tables: 6

No. of Supplementary Material Pages: 10
No. of Supplementary Figures: 4
No. of Supplementary Tables: 5

Please direct editorial correspondence and proofs to:

Dr. Ben Rozitis
Planetary and Space Sciences
School of Physical Sciences
The Open University
Walton Hall
Milton Keynes
Buckinghamshire
MK7 6AA
UK

Phone: +44 (0) 1908 332430
Fax: +44 (0) 1908 655667

Email: benjamin.rozitis@open.ac.uk

ABSTRACT

Thermal inertia is a useful property to characterise a planetary surface since it can be used as a qualitative measure of the regolith grain size. It is expected to vary with heliocentric distance because of its dependence on temperature. However, no previous investigation has conclusively observed a change in thermal inertia for any given planetary body. We have addressed this by using NEOWISE data and the Advanced Thermophysical Model to study the thermophysical properties of the near-Earth asteroids (1036) Ganymed, (1580) Betulia, and (276049) 2002 CE26 as they moved around their highly eccentric orbits. We confirm that the thermal inertia values of Ganymed and 2002 CE26 do vary with heliocentric distance, although the degree of variation observed depends on the spectral emissivity assumed in the thermophysical modelling. We also confirm that the thermal inertia of Betulia did not change for three different observations obtained at the same heliocentric distance. Depending on the spectral emissivity, the variations for Ganymed and 2002 CE26 are potentially more extreme than that implied by theoretical models of heat transfer within asteroidal regoliths, which might be explained by asteroids having thermal properties that also vary with depth. Accounting for this variation reduces a previously observed trend of decreasing asteroid thermal inertia with increasing size, and suggests that the surfaces of small and large asteroids could be much more similar than previously thought. Furthermore, this variation can affect Yarkovsky orbital drift predictions by a few tens of per cent.

Keywords:

radiation mechanisms: thermal; methods: numerical; minor planets, asteroids: individual: (1036) Ganymed, (1580) Betulia, (276049) 2002 CE26; celestial mechanics

Running head:

Varying asteroid thermal inertia

1. INTRODUCTION

1.1 Thermal inertia

Thermal inertia is a useful property for characterising an airless planetary body. As described in Rozitis & Green (2011), it can be used to infer the presence or absence of loose regolith material since it depends predominantly on regolith particle size and depth, and on the degree of compaction and exposure of solid rocks and boulders within the top few decimetres of the surface (Delbo et al. 2007). By definition, thermal inertia is a measure of a material's resistance to temperature change. It is given by $\Gamma = (k\rho C_P)^{1/2}$ where k is the thermal conductivity, ρ is the density, and C_P is the specific heat capacity of the surface layer. Increasing the thermal inertia decreases the day-side surface temperatures and increases them for the night-side of a planetary surface. Therefore, it is possible to measure the thermal inertia of a planetary surface by comparing thermal-infrared flux observations with predictions made by a thermophysical model. Such observations and models have been successfully applied to asteroids [e.g. Delbo et al. (2015) and references therein], comets (e.g. Lowry et al. 2012), the Moon (e.g. Vasavada et al. 1999), Mars (e.g. Kieffer 2013), and distant icy objects (e.g. Lellouch et al. 2013) to infer their likely surface properties.

In these thermophysical models, the three components of thermal inertia are generally considered to be constant with depth and temperature, T. However, in situ measurements of the lunar surface reveal that these properties are not constant and do vary (Keihm et al. 1973; Keihm & Langseth 1973). In particular, the temperature-dependence of thermal inertia is chiefly driven by thermal conductivity, which for a lunar-like regolith is proportional to T^3 due to the radiative transfer of heat between regolith grains (Vasavada et al. 1999).

Heat transfer in asteroid regoliths should also be dominated by the radiative component. Combining the T^3 dependence of thermal conductivity with the $r_H^{-1/2}$ dependence of equilibrium sub-solar temperature with heliocentric distance, it follows that the thermal inertia is expected to scale with heliocentric distance via $\Gamma \propto r_H^{-3/4}$ (Delbo et al. 2007). This dependence implies that thermal inertias measured for different asteroids at different heliocentric distances must be corrected to a specified heliocentric distance (typically 1 AU) to allow direct comparison. This correction is routinely applied to investigate a possible trend of decreasing thermal inertia with increasing asteroid size [e.g. see Figure 9 of Delbo et al. (2015)]. The $r_H^{-3/4}$ dependence of Γ also implies that the thermal inertia must vary around the orbit for an asteroid with high eccentricity. This variation would, in turn, have implications for accurately calculating the Yarkovsky orbital drift [e.g. see Rozitis & Green (2012) and Vokrouhlický et al. (2015) for a review] of an asteroid with high orbital eccentricity since most Yarkovsky models also assume a constant thermal inertia value.

To date, only tentative evidence has been reported for an observed variation of thermal inertia with heliocentric distance for any given small body. For instance, Marsset et al. (2017) report a thermal inertia of ~60 J m^{-2} K^{-1} $s^{-1/2}$ for the main-belt asteroid (6) Hebe from thermal-infrared data acquired at $r_H < 2.1$ AU, and ~40 J m^{-2} K^{-1} $s^{-1/2}$ from data acquired at $r_H > 2.6$ AU. However, the large uncertainties on the derived thermal inertia values overlap (i.e. they are comparable in size to the derived values), and therefore the heliocentric distance variation seen in this case is not conclusive. Additionally, Lellouch et al. (2013) report that the mean thermal inertia value for Centaurs and trans-Neptunian objects (TNOs) decreases by a factor of ~2.5 from objects measured at 8 to 25 AU (i.e. 5 ± 1 J m^{-2} K^{-1} $s^{-1/2}$) to objects measured at 41 to 53 AU (i.e. 2 ± 0.5 J m^{-2} K^{-1} $s^{-1/2}$), which is consistent with

a $\Gamma \propto r_H^{-1}$ trend expected for icy surfaces. However, this variation was obtained by comparing different groups of Centaurs/TNOs at different heliocentric distances rather than by observing changes on individual objects.

Whereas these previous studies provide hints that thermal inertia does vary with heliocentric distance as expected, they are inconclusive. A more controlled experiment would be to measure the change in thermal inertia of individual objects with significant changes in heliocentric distance. We report here a study of the thermophysical properties of the near-Earth asteroids (1036) Ganymed, (1580) Betulia, and (276049) 2002 CE26 as they move around their highly eccentric orbits. Furthermore, (1580) Betulia was observed at a similar heliocentric distance on three separate occasions, which allowed us to also check for constant thermal inertia at constant heliocentric distance.

1.2 Near-Earth asteroids (1036) Ganymed, (1580) Betulia and (276049) 2002 CE26

Detection of a change in thermal inertia of an asteroid with a high degree of confidence requires a change in thermal inertia that is larger than the thermophysical modelling uncertainties. Typically, the derived thermal inertia of an asteroid from disk-integrated observations has a relative uncertainty that is a few tens of per cent at best [e.g. see Table 2 of Delbo et al. (2015)]. This therefore requires asteroids with high orbital eccentricity, i.e. >0.4, in order to produce a big enough change in thermal inertia between perihelion and aphelion. Furthermore, suitable asteroids must also be relatively large, i.e. diameters >3 km, in order to obtain high signal-to-noise thermal-infrared measurements when at aphelion, and their shapes must be well known to minimise shape uncertainty effects on the thermal inertia derivations (e.g. Hanus et al. 2015). Finally, any suitable asteroids must also have a sufficient number of thermal-infrared measurements at differing heliocentric distances in order to constrain thermal inertia at more than one heliocentric distance. Given these criteria, a search of the radar and light-curve derived asteroid shape models, and of the NEOWISE database of asteroid sightings, was performed to identify suitable candidates. The three candidates found were the near-Earth asteroids (1036) Ganymed, (1580) Betulia, and (276049) 2002 CE26, which all have highly eccentric orbits, well-defined shape models, and multiple sightings by NEOWISE (see Figure 1 and Table 1 for a comparison of their shape models and physical properties, respectively). A brief summary of each asteroid is given below.

(1036) Ganymed (hereafter referred to as Ganymed) is the largest asteroid in the near-Earth population (i.e. effective diameter of 36 km), and has an orbital semimajor axis and eccentricity of 2.66 AU and 0.53, respectively. It is an S-type asteroid (Bus & Binzel 2002), and exhibits OH absorption features near 3 μm in several near-infrared spectral observations obtained by NASA's IRTF telescope between 10 June 2011 and 30 January 2012 (Rivkin et al. 2018). Optical light-curve measurements of Ganymed extend from 1985 to 2012 and, through light-curve inversion, constrain its rotation period, pole orientation, and shape (Hanus et al. 2015). Ganymed was observed by the cryogenic phase of the NEOWISE mission on 15-16 January 2010 and on 22-23 June 2010 when it was at heliocentric distances of 3.9 and 3.5 AU, respectively (Mainzer et al. 2011). Hanus et al. (2015) used these observations in a thermophysical model with their light-curve derived shape to obtain a thermal inertia of 35 $^{+10}/_{-5}$ J m^{-2} K^{-1} s$^{-1/2}$ at an average 3.7 AU heliocentric distance. Interestingly, Rivkin et al. (2018) estimate a thermal inertia of 214 ± 80 J m^{-2} K^{-1} s$^{-1/2}$ at an average 1.5 AU heliocentric distance from beaming parameters obtained in NEATM (Harris 1998) fits to their

near-infrared observations using the methodology of Harris & Drube (2016). Although different methods were used to obtain these two different thermal inertia values, they do suggest that Ganymed might have a strong heliocentric distance dependence of thermal inertia. In order to confirm this, we have used additional observations obtained by NEOWISE during its non-cryogenic reactivation mission on 14-15 February 2015 and on 19-20 July 2015 (Nugent et al. 2015, 2016) when Ganymed was at heliocentric distances of 3.0 and 2.1 AU, respectively. The reactivated NEOWISE mission also observed Ganymed on 4-5 January 2014 and on 12-13 June 2014 but those datasets are not used in this work due to the limited number and low signal-to-noise of the measurements. Additional thermal-infrared observations of Ganymed were obtained by Veeder et al. (1989) on 12 March 1983, by IRAS on 27 May 1983 (Tedesco et al. 2002), and by AKARI on 11-12 July 2006 (Usui et al. 2011), but again these are not used because they are limited in number and/or signal-to-noise. A summary of the four different datasets used in this work for Ganymed is given in Table 2.

(1580) Betulia (hereafter referred to as Betulia) is a 5.4-km C-type asteroid with orbital semimajor axis and eccentricity of 2.20 AU and 0.49, respectively. Historically, Betulia was well known for its unusual light-curve, which changed dramatically with solar phase angle as a result of its irregular shape (Tedesco et al. 1978). Furthermore, thermal-infrared observations obtained on 22-23 May 1976 and thermal modelling indicated that Betulia must have a high thermal inertia surface, consistent with bare rock (Lebofsky et al. 1978), in order to produce a diameter that agreed with radar and optical polarization observations (Pettengill et al. 1979; Tedesco et al. 1978). More recently, Kaasalainen et al. (2004) used optical light-curve measurements from 1976 to 1989 to constrain Betulia's rotation period, pole orientation, and shape through light-curve inversion. Harris et al. (2005) obtained additional thermal-infrared data of Betulia on 2 and 5 June 2002 using NASA's IRTF telescope. They used these measurements in a thermophysical model with the light-curve derived shape to obtain a low thermal inertia of 180 ± 50 J m^{-2} K^{-1} s$^{-1/2}$ at a heliocentric distance of 1.1 AU. They found it difficult to reconcile their results with the earlier work of Lebofsky et al. (1978), which questions the accuracy of the earlier thermal-infrared observations. Subsequently, Magri et al. (2007) produced a high resolution shape model of Betulia from inversion of radar images taken in May-June 2002. The radar shape model resembles the Kaasalainen et al. (2004) light-curve shape model but it is dominated by a prominent concavity in the southern hemisphere. The Spitzer Space Telescope (Werner et al. 2004) observed Betulia on 11 March 2005 using its InfraRed Spectrograph (IRS; Houck et al. 2004) at wavelengths ranging from 5 to 38 μm (AORKEY 4868608; Cruikshank & Van Cleve 2004). There are no reported results from this observation but an extracted spectrum is available from the Combined Atlas of Sources with Spitzer IRS Spectra (CASSIS) database (Lebouteiller et al. 2011). Betulia was at a heliocentric distance of 1.9 AU during this Spitzer observation. Finally, the reactivated NEOWISE mission observed Betulia on 23-27 October 2014, 6-7 February 2015, 20-23 May 2015, and 15-17 June 2015 (Nugent et al. 2015, 2016) when it was at heliocentric distances of 2.2, 1.6, 1.1, and 1.2 AU, respectively. Unfortunately, the NEOWISE observations obtained on October 2014 and February 2015 were taken during a time when Betulia was illuminated close to pole-on by the Sun due to its high 118° obliquity. Such 'pole-on' observations do not allow strong constraints to be obtained on an asteroid's thermal inertia value (e.g. see Rozitis 2017). Nevertheless, the June 2002, May 2015, and June 2015 thermal-infrared observations, which were obtained at similar heliocentric distances, allow an important test to check for constant thermal inertia at constant heliocentric distance. They also allow a consistency check of

thermal inertia values derived from ground-based observations with thermal inertia values derived from NEOWISE observations. A summary of the four different datasets used in this work for Betulia is given in Table 2. The Lebosky et al. (1978) dataset mentioned above is not used because of questions of its accuracy.

(276049) 2002 CE26 (hereafter referred to as 2002 CE26) is a 3.5-km binary asteroid with orbital semimajor axis and eccentricity of 2.23 AU and 0.56, respectively. Radar observations obtained on August-September 2002 reveal a primary with a highly spheroidal shape and a relatively fast spin rate of 3.29 hr, and they also reveal a relatively small companion with a diameter of 0.3 km and an orbital period of 15.6 hr (Shepard et al. 2006). The orbital configuration and size allow the bulk density of the binary system to be constrained as 900 $^{+500}/_{-400}$ kg m^{-3}. In combination with 2002 CE26's C-type spectrum (Shepard et al. 2006), this bulk density suggests that 2002 CE26 is a rubble-pile asteroid that is spinning close to or at its spin disruption limit (see Figure 1). 2002 CE26 was observed by the cryogenic phase of the NEOWISE mission on 11-13 July 2010 when it was at a heliocentric distance of 3.0 AU (Mainzer et al. 2011). It was also observed by the reactivated NEOWISE mission on 1-2 June 2014, 30-31 December 2014, and 16-18 April 2015 when it was at heliocentric distances of 1.8, 1.3, and 2.1 AU, respectively (Nugent et al. 2015, 2016). Similar to Betulia, the NEOWISE observations obtained on April 2015 were taken during a time when 2002 CE26 was illuminated close to pole-on by the Sun due to its high 122° obliquity, and therefore those observations cannot be used to constrain its thermal inertia at that time. Shepard et al. (2006) also obtained a near-infrared spectrum of 2002 CE26 with NASA's IRTF telescope on 29 August 2004. The long wavelength portion of the near-infrared spectrum was dominated by thermal flux, which Shepard et al. (2006) fit with NEATM to derive a beaming parameter of 0.92 at a solar phase angle of 28°. Unlike Ganymed, which Rivkin et al. (2018) observed over a range of phase angles, this single beaming parameter value for 2002 CE26 is insufficient to obtain a reliable thermal inertia value using the methodology of Harris & Drube (2016). A summary of the three different datasets used in this work for 2002 CE26 is given in Table 2.

The thermal inertia of each asteroid at each heliocentric distance mentioned above can be determined by using their respective shape models in the Advanced Thermophysical Model (Rozitis & Green 2011, 2012, 2013) to predict and compare the thermal flux emitted by the asteroids at each observing epoch. This analysis is described in detail in Section 2, a discussion of the results is given in Section 3, and a summary with conclusions is provided in Section 4. Additionally, Appendix A describes in detail how reflected solar radiation is removed from the near-infrared thermal flux observations of Ganymed, and Appendix B verifies a new rotationally averaged flux fitting technique that can be applied to spheroidal shaped asteroids such as 2002 CE26. Finally, supplementary figures and tables referred to in the text are provided online.

2. THERMOPHYSICAL MODELLING

2.1 The Advanced Thermophysical Model

The Advanced Thermophysical Model (or ATPM for short) is used to compute the thermal inertia of Ganymed, Betulia, and 2002 CE26 as a function of heliocentric distance from measured thermal-infrared fluxes. The ATPM was developed to interpret thermal-infrared observations of airless planetary surfaces, and to simultaneously make asteroidal Yarkovsky and YORP effect predictions (Rozitis & Green 2011, 2012, 2013). It has been previously used to measure the thermal inertia of four near-Earth asteroids: (1620) Geographos (Rozitis & Green 2014); (1862) Apollo (Rozitis et al. 2013); (29075) 1950 DA (Rozitis et al. 2014); and (175706) 1996 FG3 (Wolters et al. 2011).

The ATPM computes the surface temperature distribution, and thermal emission, of an asteroid using specified thermophysical properties such as the Bond albedo, thermal inertia, surface roughness, rotation state, and shape. In particular, the one-dimensional conduction equation is solved for each triangular facet of a shape model (derived from radar observations or light-curve inversion) to determine the surface temperature variation as the asteroid rotates. The surface boundary condition for each facet is the energy balance between incoming radiation (direct solar illumination plus scattered sunlight and re-emitted thermal emission from interfacing facets) and emitted energy (thermal emission and conduction). Roughness, on scales smaller than the facet size, but larger than the thermal skin depth (~cm), is incorporated through the fractional coverage of hemispherical craters on a smooth surface. The roughness fraction f_R, has a value of zero for a fully smooth surface and unity for a fully rough surface. The hemispherical crater (i.e. with crater opening angle of 180°) reproduces the thermal-infrared beaming effects of different surface roughness morphologies, and accurately reproduces the beaming effect measured for the Moon (Rozitis & Green 2011; Davidsson et al. 2015) using the single parameter f_R. The total emitted thermal flux is derived from the sum of the Planck function for all facets visible to the observer for any specified rotation phase.

2.2 Thermal-infrared data retrieval

All instances of NEOWISE observations of Ganymed, Betulia, and 2002 CE26 were taken from the Minor Planet Center database and used to query the WISE All-Sky Single Exposure (L1b) source database for the cryogenic observations, and the NEOWISE-R Single Exposure (L1b) source database for the non-cryogenic observations, via the NASA/IPAC Infrared Service Archive. These databases were queried in their moving object search modes by specifying the asteroid of interest in the single object search entry, and by specifying the range of dates applicable for each observational epoch in the observation begin and end time entries. These queries were also performed with a moving object match radius of 5''. The magnitudes returned from these queries were kept only in the instances in which there was a positive object detection at the 3-σ level or greater, and when the measured object position was within 1'' of its predicted position. The WISE magnitudes were converted to fluxes, and the reported red–blue calibrator discrepancy was taken into account (Wright et al. 2010). A 2.8%, 4.5%, and 5.7% uncertainty was also added in quadrature to the reported observational uncertainties to take into account additional calibration uncertainties in the W2 (4.6 μm), W3 (11.1 μm), and W4 (22.6 μm) channels, respectively (Jarrett et al. 2011). As in our previous work for 1950 DA (Rozitis et al. 2014), we colour-correct the model fluxes using the WISE

corrections of Wright et al. (2010) rather than colour-correcting the observed fluxes. A summary of the number of flux measurements obtained for each observational epoch is given in Table 2.

The NASA IRTF fluxes of Betulia used in this work were obtained from Table 2 of Harris et al. (2005). Harris et al. (2005) mention that the reported uncertainties for their measurements are only statistical uncertainties that result from the photometry of their thermal-infrared images, and do not include absolute calibration uncertainties. For other ground-based thermal-infrared observations, the absolute calibration uncertainty is estimated to range from 7% to 10% (Lim et al. 2005; Wolters et al. 2008), and so we took the mid-range and added an additional 8.5% uncertainty in quadrature to the reported observational uncertainties.

The extracted Spitzer IRS spectrum of Betulia was downloaded from the CASSIS database (Lebouteiller et al. 2011). To account for flux offsets in the different wavelength modules, the observed flux was multiplied by a factor of 0.985, 0.973, 1.005 and 1.036 in the SL2 (5.2-7.6 μm), SL1 (7.4-14.2 μm), LL2 (14-21 μm), and LL1 (21-40 μm) modules, respectively. The absolute calibration uncertainty in each module is 10% or less (Decin et al. 2004), and so the overall uncertainty for the four modules combined is 5% (Hanus et al. 2016). This absolute calibration uncertainty is taken into account in the analysis described in Section 2.4.2.

After acquiring all the relevant observations, the data point fluxes in each dataset were scaled to the common geometries given in Table 2 to remove changing geometry effects within each dataset (i.e. an adjustment at the few per cent level).

2.3 Thermal-infrared flux fitting

In a typical thermophysical model fit to thermal-infrared observations of an asteroid, the free parameters to be constrained include the effective diameter (i.e. the equivalent diameter of a sphere with the same volume as the irregularly shaped asteroid), D, thermal inertia, Γ, surface roughness, f_R, and also the rotation phase, φ, if necessary. Depending on the asteroid and the dataset to be fitted, some of these parameters were kept fixed in the model fitting, and the list of fixed and free parameters used for each asteroid and dataset is described in detail in Section 2.4. For each model fit, the thermal flux predictions, $F_{MOD}(\lambda_n,\varphi_n,D,\Gamma,f_R)$, were compared with the observations, $F_{OBS}(\lambda_n,\varphi_n)$, and observational errors, $\sigma_{OBS}(\lambda_n,\varphi_n)$, by varying the relevant free parameters to give the minimum χ^2 fit,

$$\chi^2 = \sum_{n=1}^{N} \frac{[FCF(D)F_{MOD}(\lambda_n,\phi_n,D,\Gamma,f_R) - F_{OBS}(\lambda_n,\phi_n)]^2}{\sigma_{MOD}(\lambda_n,\phi_n,D,\Gamma,f_R)^2 + \sigma_{OBS}(\lambda_n,\phi_n)^2},$$ (1)

for a set of n = 1 to N observations with wavelength λ_n. For asteroids with datasets where the rotational phase was difficult to constrain, an additional model uncertainty, $\sigma_{MOD}(\lambda_n,\varphi_n,D,\Gamma,f_R)$, was added in quadrature to the observational uncertainty. This model uncertainty was calculated by evaluating the standard deviation of the model flux about its average value over a given range of rotation phase. $FCF(D)$ is a flux correction factor that took into account variable Bond albedo (Wolters et al. 2011; Rozitis et al. 2013), and is given by

$$FCF(D) = \frac{1 - A_B(D)}{1 - A_{B\_MOD}},$$ (2)

where $A_B(D)$ is the required Bond albedo for an asteroid with effective diameter D, and A_{B_MOD} is the model Bond albedo used in the ATPM. This flux correction factor saves computational effort by not running the thermophysical model for every Bond albedo required. Model Bond albedo values of 0.11, 0.03, and 0.01 were used for the thermophysical modelling of Ganymed, Betulia, and 2002 CE26, respectively. These values were calculated by using the Fowler & Chillemi (1992) methodology with the absolute visual magnitudes, phase parameters, and effective diameters given in Table 1. Typically, the flux correction factor was within 10% of unity when using these model Bond albedo values.

A bolometric emissivity of 0.9 was assumed in the thermal model temperature calculations, and a spectral emissivity of 0.9 was also assumed at all observed wavelengths in the thermal flux calculations. These appear to be good assumptions for the emissivity since thermophysical models can reproduce ~4 to ~40 μm observations of the S-type asteroid (25143) Itokawa (Müller et al. 2014), the B-type asteroid (101955) Bennu (Emery et al. 2014), and the C-type asteroid (162173) Ryugu (Müller et al. 2017) when using them. However, we do investigate the influence of the spectral emissivity in the analysis of the W2 channel data since laboratory measurements of silicate materials show increased spectral reflectance, and hence reduced spectral emissivity, at wavelengths of less than ~8 μm (e.g. Wan et al. 1994; Snyder et al. 1997; Baldridge et al. 2009).

For each observational epoch/dataset, thermophysical models were run using the asteroid shape models shown in Figure 1 with the previously measured properties listed in Table 1 and the observational geometry listed in Table 2. The thermal inertia was varied between 0 and 200 J m^{-2} K^{-1} s$^{-1/2}$ in equally spaced steps of 5 J m^{-2} K^{-1} s$^{-1/2}$ for Ganymed, and between 0 and 500 J m^{-2} K^{-1} s$^{-1/2}$ in equally spaced steps of 10 J m^{-2} K^{-1} s$^{-1/2}$ for Betulia and 2002 CE26. The roughness fractions were also stepped through their plausible ranges to form a 2D grid of model test parameters (or clones). In cases where the effective diameter, or rotation phase, was also left as a free parameter to be fitted, this became a 3D grid of model test parameters. After a minimum χ^2 fit for a particular dataset was found, a parameter region bounded by a constant $\Delta\chi^2$ value at the 3-σ confidence level (i.e. $\Delta\chi^2$ = 11.8 or 14.2 for 2 or 3 free parameters, respectively) then defined the range of possible parameters/clones. As in Wolters et al. (2011), all acceptable clones were then averaged to give a mean and standard deviation of the free parameters fitted to characterise the results of the model fit to that particular dataset. In Section 2.4.1, we also checked that the uncertainties derived for Ganymed using this methodology were realistic by employing the bootstrap method.

2.4 Results

2.4.1 (1036) Ganymed

The two sets of NEOWISE observations obtained in January and June 2010 during the cryogenic phase of the mission included data from the mid-infrared W3 and W4 channels, as well as data from the shorter wavelength W1 (3.4 μm) and W2 channels. The W1 and W2 channels contained a large amount of reflected solar radiation due to Ganymed's S-type albedo and cool temperature at high heliocentric distance, and therefore, like Hanus et al. (2015), we only fitted the W3 and W4 channels to derive the thermal inertia on those dates. The free parameters in those fits were the diameter, thermal inertia, and surface roughness. The accuracy of Ganymed's rotation period was sufficiently high to allow rotational phasing of its light-curve derived shape model with the NEOWISE observations, and therefore the rotational phase was a pre-computed and fixed parameter.

The ATPM fit to the January 2010 dataset gave an effective diameter of 35.7 ± 1.2 km, a thermal inertia of 24 ± 8 J m^{-2} K^{-1} s$^{-1/2}$, and a surface roughness of 0.83 ± 0.13 with a model fit reduced-χ^2 of 0.68 for a heliocentric distance of 3.90 AU. Likewise, the ATPM fit to the June 2010 dataset gave an effective diameter of 36.0 ± 1.0 km, a thermal inertia of 31 ± 13 J m^{-2} K^{-1} s$^{-1/2}$, and a surface roughness of 0.77 ± 0.16 with a model fit reduced-χ^2 of 0.39 for a heliocentric distance of 3.46 AU. The ATPM fits to these two datasets are displayed in the lower two panels of Figure 2. These results compare well to an effective diameter of 36 ± 1 km and a thermal inertia of 35 $^{+10}/_{-5}$ J m^{-2} K^{-1} s$^{-1/2}$ obtained by Hanus et al. (2015) who fitted both datasets simultaneously. The low reduced-χ^2 value (i.e. <0.5) of the fit to the June 2010 observations indicates that the flux uncertainties for this dataset are possibly too large and/or the ATPM fit has too many free parameters. However, the low relative scatter of the flux data points shown in Figure 2 suggests that it is the former case of the flux uncertainties being too large.

Unlike the cryogenic mission phase, the two sets of NEOWISE observations obtained in February and July 2015 during the reactivated non-cryogenic mission phase included data from only the W1 and W2 channels. While the W1 channel still predominantly contained reflected solar radiation, with Ganymed at a smaller heliocentric distance, the W2 channel was dominated by emitted thermal radiation. Therefore, it was possible to derive thermal inertia from the W2 channel data only for those two datasets. Single wavelength observations do not usually allow unique constraints on the diameter, thermal inertia, and surface roughness because of a strong degeneracy between these parameters when using one wavelength. Fortunately, such degeneracy can be broken when an independent diameter constraint is available (e.g. from radar observations or spacecraft imaging), which allows the diameter to be varied within a narrow range during the model fitting (Nugent 2013). For example, this method was used for 1950 DA in Rozitis et al. (2014). For Ganymed, a tight diameter constraint was available from the ATPM fits to the January and June 2010 observations, which was also in good agreement with the diameter obtained by Hanus et al. (2015). Therefore, the free parameters that were constrained by fits to the February and July 2015 observations were just the thermal inertia and surface roughness.

Before ATPM could be fitted to the W2 channel data, the reflected solar radiation component still needed to be removed. Appendix A describes in detail the methodology used for calculating the reflected solar radiation component from knowledge of Ganymed's absolute magnitude H and phase slope G, and from measurements of its reflectance properties at 4.6 μm, i.e. the reflectance ratio $p_{4.6\mu m}/p_V$. In summary, it was found that the thermal component contribution to the total observed flux was 42.6 ± 6.2 and 82.2 ± 1.8 per cent during the February and July 2015 observations, respectively, when assuming a spectral emissivity at 4.6 μm of 0.9. Therefore, the measurements in the W2 channel were multiplied by these factors to give the observed thermal flux to be fitted. The use of a multiplying factor rather than a constant flux offset ensured that the thermal light-curves retained their relative amplitudes during conversion. The uncertainties in the multiplying factors meant that the thermal fluxes had systematic uncertainties of 14.6 and 2.2 per cent during the February and July 2015 observations, respectively. These systematic uncertainties translate to an additional diameter uncertainty of 7.3 and 1.1 per cent, respectively, and the allowable diameter range in the ATPM fitting described above was expanded accordingly.

Using the above modifications for the W2 channel observations, the ATPM fit to the February 2015 dataset gave a thermal inertia of 47 ± 14 J m^{-2} K^{-1} s$^{-1/2}$ and a surface roughness of 0.66

± 0.23 with a model fit reduced-χ^2 of 0.59 for a heliocentric distance of 2.99 AU. Likewise, the ATPM fit to the July 2015 dataset gave a thermal inertia of 96 ± 21 J m^{-2} K^{-1} s$^{-1/2}$ and a surface roughness of 0.71 ± 0.19 with a model fit reduced-χ^2 of 0.67 for a heliocentric distance of 2.09 AU. The ATPM fits to these two datasets are displayed in the upper two panels of Figure 2.

To summarise the above results, Ganymed had thermal inertias of 96 ± 21, 47 ± 14, 31 ± 13, and 24 ± 8 J m^{-2} K^{-1} s$^{-1/2}$ (uncertainties given are 1-σ) for heliocentric distances of 2.09, 2.99, 3.46, and 3.90 AU, respectively. These measurements show that the thermal inertia of Ganymed did vary with heliocentric distance when a spectral emissivity at 4.6 μm of 0.9 was assumed. As demonstrated in Figure 2, the low thermal inertia values that fitted data at high heliocentric distances produced flux predictions that were too high at small heliocentric distances because they potentially made Ganymed too hot. Likewise, the high thermal inertia values that fitted data at small heliocentric distances produced flux predictions that were too low at high heliocentric distances because they potentially made Ganymed too cold. Combining the χ^2 values for the best individual fits at each observational epoch produced an overall reduced-χ^2 value of 0.56 for ten free parameters (i.e. 2 diameters, 4 thermal inertia values, and 4 surface roughness values). Trying to fit all four datasets simultaneously with just three free parameters (i.e. diameter, thermal inertia, and surface roughness) produced a large reduced-χ^2 of 4.61 because a single set of thermal inertia and surface roughness values could not adequately fit all of the data in the presence of these flux offsets. Figure 3 demonstrates that the thermal inertia values which provided the best χ^2 fit for each dataset are clearly offset from one another at identical degrees of surface roughness. However, there was still some overlap in the derived thermal inertia values, especially for those nearby in terms of heliocentric distance. This overlap is mainly a consequence of the known degeneracy of thermal inertia with surface roughness when fitting thermal-infrared data [e.g. see Rozitis (2017) for a detailed explanation]. The lower thermal inertia bounds tend to come from low roughness, and the higher thermal inertia bounds tend to come from high roughness. Therefore, the upper thermal inertia bound of one measurement may not necessarily agree with the lower bound of a neighbouring thermal inertia measurement in terms of their degrees of surface roughness.

To investigate the sensitivity of the results to the spectral emissivity at 4.6 μm, the analysis for the February and July 2015 observations was repeated using different assumed values for the spectral emissivity, and Table 3 summarises the results. As shown, lowering the 4.6 μm spectral emissivity lowers the thermal inertia derived for these observations, and also lowers the reduced-χ^2 value of the four dataset simultaneous fit. However, even at the lowest spectral emissivity tested (i.e. 0.6) there was still a residual trend of decreasing thermal inertia with increasing heliocentric distance. Therefore, a low 4.6 μm spectral emissivity cannot fully account for the variation in thermal inertia seen within these four datasets. An investigation of the near-infrared spectral emissivity of S-type asteroids is needed in order to precisely say which set of thermal inertia values are representative of Ganymed. However, as mentioned previously, we note that Müller et al. (2014) were able to reproduce the ~4 to ~40 μm observations of the S-type asteroid Itokawa using the standard assumption that the spectral emissivity was 0.9 at all observed wavelengths within their thermophysical model.

To determine whether the thermal inertia uncertainties derived above were realistic, we performed an alternative analysis using the bootstrap method for comparison with our results. For the January and June 2010 observations, the data were re-sampled to produce one thousand

different datasets for fitting with the ATPM. In each bootstrap trial, the W3 and W4 channel data were randomly selected from Gaussian distributions centred on the measured values with widths equal to the measurement uncertainties. The minimum χ^2 fit for each bootstrap trial was found using the ATPM, and the parameters that provided the best fit for each trial were then averaged to give the mean and standard deviation of the overall model fit. The bootstrap analysis of the January 2010 dataset gave an effective diameter of 35.8 ± 1.8 km, a thermal inertia of 27 ± 6 J m^{-2} K^{-1} s$^{-1/2}$, and a surface roughness of 0.97 ± 0.07. Likewise, the bootstrap analysis of the June 2010 dataset gave an effective diameter of 35.8 ± 1.7 km, a thermal inertia of 34 ± 9 J m^{-2} K^{-1} s$^{-1/2}$, and a surface roughness of 0.87 ± 0.14. These results compare well to those obtained previously when using the standard method described above and, except for the effective diameter, the derived uncertainties were generally smaller.

For the February and July 2015 observations, the W2 channel data was also re-sampled one thousand times using the measurement uncertainties. Systematic offsets were applied to the re-sampled data in order to take into account the systematic uncertainties of the W2 channel data described previously. These systematic offsets were randomly selected from Gaussian distributions with mean values of 1, and with widths of 0.146 and 0.022 for the February and July 2015 observations, respectively. In each bootstrap trial, the effective diameter of Ganymed was also randomly selected from a Gaussian distribution. Based on the bootstrap analysis for the January and June 2010 observations, this Gaussian distribution had a mean value of 35.8 km with a width of 1.7 km. The bootstrap analysis was repeated for each value of the 4.6 μm spectral emissivity, and Supplementary Table S1 summarises the results. Again, the bootstrap analysis produced thermal inertia values and uncertainties that were in good agreement with the standard method described above. Based on this alternative analysis, the derived uncertainties using our standard method are realistic for the thermal inertia studies presented in this work.

2.4.2 (1580) Betulia

The two sets of NEOWISE observations obtained during the reactivated non-cryogenic mission phase on May and June 2015 returned many data points in the W2 channel that sampled the thermal light-curves of Betulia very well. As Betulia is a C-type asteroid with a low albedo, the reflected solar radiation component contributed a negligible amount to the total W2 channel flux (i.e. <1% contribution), and so this channel essentially measured Betulia's thermal emission only. Therefore, unlike Ganymed, no adjustments to the measured flux in the W2 channel were needed for ATPM fitting. The free parameters in these fits were the thermal inertia, surface roughness, and rotation phase. An additional diameter constraint could not be obtained by using just the W2 channel on its own. Fortunately, the radar observations and shape model of Betulia placed a strong constraint on its diameter (Magri et al. 2007), and therefore it was varied within its previously measured range of 5.39 ± 0.54 km in the ATPM fitting. It was necessary to leave the rotation phase as a free parameter because the rotation period of Betulia is not known with sufficient accuracy to allow rotational phasing of the radar observations taken in 2002 with the NEOWISE observations obtained in 2015.

Using these free parameters, the ATPM fit to the May 2015 dataset gave a thermal inertia of 200 ± 10 J m^{-2} K^{-1} s$^{-1/2}$ and a surface roughness of 0.79 ± 0.05 with a model fit reduced-χ^2 of 1.39 for a heliocentric distance of 1.13 AU. Likewise, the ATPM fit to the June 2015 dataset gave a thermal inertia of 189 ± 30 J m^{-2} K^{-1} s$^{-1/2}$ and a surface roughness of 0.78 ± 0.08 with a model fit reduced-χ^2 of

2.13 for a heliocentric distance of 1.16 AU. The ATPM fits to these two datasets are displayed in the left panels of Figure 4, and Supplementary Figure S1 shows the χ^2 fitting results. As shown in Figure 4, there was a good agreement between the thermal light-curves predicted by the ATPM using the Betulia shape model with those measured by NEOWISE.

The Spitzer IRS observations of Betulia were modelled using the same free parameters as used for the NEOWISE observations described above. The 5% absolute calibration uncertainty of the Spitzer IRS observations described in Section 2.2 translated to a 2.5% uncertainty in diameter, and the allowable diameter range of Betulia was expanded accordingly. The ATPM fit to this dataset gave a thermal inertia of 175 ± 51 J m^{-2} K^{-1} s$^{-1/2}$ and a surface roughness of 0.76 ± 0.18 with a model fit reduced-χ^2 of 0.25 for a heliocentric distance of 1.92 AU. The bottom right panel of Figure 4 displays the ATPM fit to this dataset. Again, the low reduced-χ^2 value obtained here indicates that the flux uncertainties are possibly too large. Indeed, the total flux uncertainties provided by the CASSIS database included an RMS component and a systematic component with approximately equal contributions (Lebouteiller et al. 2011). Ignoring the systematic component would produce a reduced-χ^2 value of ~1. The larger thermal inertia uncertainty obtained here, as compared to the NEOWISE thermal inertia constraints, results from the Spitzer IRS observations being taken at a single unknown rotation phase that could not be constrained in the ATPM fitting. However, the wavelength coverage and resolution of the Spitzer IRS observations does allow the emissivity spectrum of Betulia to be extracted. This extraction was performed by dividing the observations by the best model fit, and then multiplying by the assumed emissivity of 0.9. Figure 5 displays the extracted emissivity spectrum of Betulia for wavelengths ranging from 5 to 38 μm. As shown, a spectral emissivity of 0.9 is a good assumption across all observed wavelengths due to the very little variability in emissivity seen here.

The above thermal inertia values are consistent with the 180 ± 50 J m^{-2} K^{-1} s$^{-1/2}$ measured by Harris et al. (2005) using NASA IRTF data obtained at a heliocentric distance of 1.15 AU. As additional consistency checks, we also modelled the NASA IRTF data using both the radar shape model we've used so far and the light-curve shape model used in Harris et al. (2005). For the light-curve shape model, we left the diameter as a free parameter, in addition to the previous three free parameters, to determine if the radar-derived diameter was reproducible in the model fitting. The ATPM fit gave a diameter of 5.58 ± 0.26 km, a thermal inertia of 167 ± 54 J m^{-2} K^{-1} s$^{-1/2}$, and a surface roughness of 0.75 ± 0.19 with a model fit reduced-χ^2 of 1.13. The derived diameter was in good agreement with the radar-derived value of 5.39 ± 0.54 km, and indicated that the radar shape model was reliable for thermophysical modelling (Rozitis & Green 2014). Furthermore, our derived thermal inertia value and its uncertainty were in good agreement with that of Harris et al. (2005). In comparison, the ATPM fit using the radar shape model with its diameter constraint gave a thermal inertia of 195 ± 37 J m^{-2} K^{-1} s$^{-1/2}$ and a surface roughness of 0.67 ± 0.24 with a model fit reduced-χ^2 of 1.09. The ATPM fit to the NASA IRTF dataset is displayed in the top right panel of Figure 4.

To summarise the above results, Betulia had thermal inertias of 200 ± 10, 195 ± 37, 189 ± 30, and 175 ± 51 J m^{-2} K^{-1} s$^{-1/2}$ for heliocentric distances of 1.13, 1.15, 1.16, and 1.92 AU, respectively. The first three measurements confirm that the thermal inertia of Betulia is indeed constant at constant heliocentric distance (see Supplementary Figure S1). The agreement between the NEOWISE results and the NASA IRTF results provides confidence in thermal inertia values obtained by thermophysical modelling of NEOWISE data. Additionally, the agreement in results between those

produced by the ATPM and the model of Harris et al. (2005) adds further confidence that reproducible thermal inertia values can be obtained. Although lower than the first three measurements, the fourth measurement at a higher heliocentric distance doesn't strongly indicate a change in thermal inertia due to its relatively large uncertainty. However, this fourth measurement sampled a significantly different region of Betulia's surface to that of the other three measurements (see Table 2). As shown in Supplementary Figure S1, there is a greater degeneracy between thermal inertia and surface roughness for the observation geometry of these Spitzer observations. If the surface roughness over the observable illuminated region in the southern hemisphere (which dominates the thermal flux) is lower than the average roughness for the northern/equatorial latitudes illuminated at the other three observations dates, then the thermal inertia would be correspondingly lower. It was not possible to fit all four datasets simultaneously because the rotation period of Betulia was not known with sufficient accuracy to rotationally phase the four sets of observations.

To investigate the sensitivity of the results to the spectral emissivity at 4.6 µm, the analysis for the May and June 2015 observations was repeated using different assumed values for the spectral emissivity, and Supplementary Table S2 summarises the results. Like Ganymed, lowering the 4.6 µm spectral emissivity lowers the thermal inertia derived for these observations. However, lowering these thermal inertia values makes them inconsistent with the thermal inertia value derived from the longer wavelength NASA IRTF observations obtained at a similar heliocentric distance. In combination with the emissivity spectrum extracted from the Spitzer IRS observations, it seems that a spectral emissivity of 0.9 is a good assumption for all wavelengths ranging from ~4 to ~40 µm. This finding is in agreement with Emery et al. (2014) and Müller et al. (2017) who were able to reproduce the ~4 to ~40 µm observations of the B-type asteroid Bennu and the C-type asteroid Ryugu, respectively, by using the standard assumption that the spectral emissivity was 0.9 at all observed wavelengths in their thermophysical models. As discussed in Emery et al. (2014), the low albedo of these asteroids seems to reduce the contrast of their spectral emissivity variations.

2.4.3 (276049) 2002 CE26

The set of NEOWISE observations obtained during the cryogenic phase of the mission on July 2010 included data from the W3 channel only. Similarly, the two sets of NEOWISE observations obtained during the reactivated non-cryogenic mission phase on June and December 2014 included data from the W2 channel only. Like Betulia, 2002 CE26 is a C-type asteroid where the reflected solar radiation component contributed a negligible amount to the total flux measured in both channels (i.e. <1% contribution), and therefore no adjustments were needed to the measured flux for ATPM fitting. The free parameters to be constrained by fits to the NEOWISE data included the thermal inertia and surface roughness for each dataset. The diameter of 2002 CE26 was varied within its radar-derived range of 3.5 ± 0.4 km (Shepard et al. 2006). The rotation phase was not included as a free parameter because 2002 CE26 has a highly spheroidal shape and exhibited very low amplitude thermal light-curves. Instead, we fitted the rotationally averaged model flux to the data, and the standard deviation of the small rotational variation in flux (i.e. ~1-3%) was added in quadrature to the measured flux uncertainties. Appendix B tests and confirms the validity of this method by using the NEOWISE data of 1950 DA previously studied in Rozitis et al. (2014). The flux emitted by the small secondary asteroid of 2002 CE26 was also neglected because it contributed less than one per cent to the total observed flux.

Using these free parameters, the ATPM fit to the July 2010 dataset gave a thermal inertia of 54 ± 27 J m^{-2} K^{-1} s$^{-1/2}$ and a surface roughness of 0.54 ± 0.30 with a model fit reduced-χ^2 of 0.30 for a heliocentric distance of 2.98 AU. The low reduced-χ^2 value obtained here again indicates that the flux uncertainties are possibly too large, which is also implied by the low relative scatter of the flux data points seen in Figure 6. The ATPM fit to the June 2014 dataset gave a thermal inertia of 102 ± 30 J m^{-2} K^{-1} s$^{-1/2}$ and a surface roughness of 0.52 ± 0.30 with a model fit reduced-χ^2 of 1.96 for a heliocentric distance of 1.84 AU. Finally, the ATPM fit to the December 2014 dataset gave a thermal inertia of 167 ± 33 J m^{-2} K^{-1} s$^{-1/2}$ and a surface roughness of 0.23 ± 0.18 with a model fit reduced-χ^2 of 4.10 for a heliocentric distance of 1.32 AU. The large reduced-χ^2 value obtained here indicates that the ATPM and/or the flux uncertainties are not adequately representing the scatter seen in the December 2014 data. In particular, the mean flux uncertainty for each data point was 4.0% whereas the scatter of the data points implies that it should be 8.6%. This scatter appears to be random and might be caused by 2002 CE26 traversing a dense background field of stars. Using an uncertainty of 8.6% for each flux data point produces a thermal inertia of 172 ± 34 J m^{-2} K^{-1} s$^{-1/2}$ and a surface roughness of 0.48 ± 0.30 with a reduced-χ^2 value of 1.05. We adopt this constraint, rather than the original, to avoid uncertainties that are too small. The ATPM fits to these datasets are displayed in Figure 6, and Supplementary Figure S2 shows the χ^2 fitting results. It was surprising that a thermal inertia constraint could be obtained from the six flux measurements of the June 2014 dataset. However, 2002 CE26 was in a favourable geometry that caused large differences in the predicted flux between the different thermal inertia values tested. As shown in Supplementary Figure S3, the co-variance of the fitted diameter with thermal inertia had the steepest trend for the June 2014 set of observations. This steep trend allowed the thermal inertia to be determined when the radar-derived diameter constraint was applied.

To summarise the above results, 2002 CE26 had thermal inertias of 172 ± 34, 102 ± 30, and 54 ± 27 J m^{-2} K^{-1} s$^{-1/2}$ for heliocentric distances of 1.32, 1.84, and 2.98 AU, respectively. These measurements show that the thermal inertia of 2002 CE26 did also vary with heliocentric distance when a spectral emissivity at 4.6 μm of 0.9 was assumed. As demonstrated in Figure 6, and similar to Ganymed, the low thermal inertia value that fitted the data at high heliocentric distance produced a flux prediction that was too high at small heliocentric distance because it potentially made 2002 CE26 too hot. Likewise, the high thermal inertia value that fitted the data at small heliocentric distance produced a flux prediction that was too low at high heliocentric distance because it potentially made 2002 CE26 too cold. Combining the χ^2 values for the best individual fits at each observational epoch produced an overall reduced-χ^2 value of 0.91 for six free parameters (i.e. 3 thermal inertia values and 3 surface roughness values). Trying to fit all three datasets of 2002 CE26 simultaneously with just two free parameters (i.e. thermal inertia and surface roughness) produced a larger reduced-χ^2 of 1.94 because a single set of thermal inertia and surface roughness values could not fit all of the data as well in the presence of these flux offsets.

To investigate the sensitivity of the results to the spectral emissivity at 4.6 μm, the analysis for the June and December 2014 observations was repeated using different assumed values for the spectral emissivity, and Supplementary Table S3 summarises the results. Like Ganymed and Betulia, lowering the 4.6 μm spectral emissivity lowers the thermal inertia derived for these observations, and also lowers the reduced-χ^2 value of the three dataset simultaneous fit. However, even at the lowest spectral emissivity tested there was still a residual trend of decreasing thermal inertia with increasing heliocentric distance. Since 2002 CE26 is a C-type asteroid like Betulia and Ryugu then it

would likely have a similar spectral emissivity to them, which is 0.9 for wavelengths ranging from ~4 to ~40 µm. Therefore, we consider the thermal inertia values derived from the analysis using a 4.6 µm spectral emissivity of 0.9 to be representative of 2002 CE26.

To determine if the results were sensitive to subtle variations in the shape model used, we also repeated our analysis using the dynamically equivalent and equal volume ellipsoid of 2002 CE26 (i.e. the ellipsoid has semi-axes of a = 1.80, b = 1.79, and c = 1.61 km), and obtained identical results to the analysis using the radar shape model. Therefore, our results are not sensitive to subtle uncertainties in the shape model of 2002 CE26.

2.5 Characterising the observed variation

Table 4 summarises the results of these investigations when assuming a 4.6 µm spectral emissivity of 0.9, and Figure 7 displays the results. As shown, the thermal inertia of Ganymed and 2002 CE26 did indeed decrease with heliocentric distance, and the variation appears to be more extreme than the $\Gamma \propto r_H^{-3/4}$ trend expected. The Betulia measurements confirm that thermal inertia is constant at constant heliocentric distance, but are inconclusive of a heliocentric distance variation. However, the Betulia data cover a smaller range of heliocentric distance, and could also be affected if any surface inhomogeneity was present. All of the Ganymed and 2002 CE26 observations were made with relatively similar observation and illumination geometry (see Table 2), and thus would not be affected by spatial inhomogeneities.

Using the thermal inertia measurements obtained as a function of heliocentric distance, it was possible to fit a power-law of the form

$$\Gamma = \Gamma_0 r_H^{\alpha}, \tag{3}$$

where Γ_0 is the equivalent thermal inertia at 1 AU, r_H is the heliocentric distance in AU, and α is an exponent that describes the heliocentric distance variation. As shown in Figure 8, a chi-squared fit of this power-law to the thermal inertia measurements of Ganymed gave Γ_0 = 500 $^{+670}/_{-315}$ J m^{-2} K^{-1} s$^{-1/2}$ and α = -2.22 $^{+0.88}/_{-0.90}$ when excluding the Rivkin et al. (2018) measurement, and Γ_0 = 500 $^{+400}/_{-255}$ J m^{-2} K^{-1} s$^{-1/2}$ and α = -2.22 $^{+0.68}/_{-0.66}$ when it is included. It could be argued that the Rivkin et al. (2018) measurement should be excluded from this power-law fit because it was obtained by a different and indirect method. However, the method of inverting NEATM beaming parameter values to obtain a thermal inertia value has been shown by Rivkin et al. (2018) to accurately reproduce the known thermal inertia value of (433) Eros. In either case, the Rivkin et al. (2018) measurement is consistent with the trend established by the four measurements using the NEOWISE observations with the spectral emissivity assumption given above. For 2002 CE26, a chi-squared fit of this power-law to its thermal inertia measurements gave Γ_0 = 255 $^{+165}/_{-105}$ J m^{-2} K^{-1} s$^{-1/2}$ and α = -1.46 $^{+0.86}/_{-1.22}$ (see Figure 8). For Betulia, its thermal inertia measurements still allowed a constraint to be made on its power-law parameters despite their limited range in heliocentric distance. A chi-squared fit of this power-law gave Γ_0 = 205 $^{+40}/_{-25}$ J m^{-2} K^{-1} s$^{-1/2}$ and α = -0.26 $^{+0.26}/_{-1.12}$, which indicates that both constant thermal inertia and varying thermal inertia remain possible. As shown in Figure 8, there is a covariance between α and Γ_0 in the power-law fits where low α results in high Γ_0 and high α results in low Γ_0.

To investigate the sensitivity of the power-law fits to the spectral emissivity at 4.6 μm, the fits for Ganymed and 2002 CE26 were repeated using the thermal inertia measurements obtained from different assumed values for the spectral emissivity, and Supplementary Table S4 summarises the results. As shown, lowering the 4.6 μm spectral emissivity reduces the variation of thermal inertia with heliocentric distance for both asteroids. However, even at the lowest spectral emissivity tested (i.e. 0.6) there was still a residual trend of decreasing thermal inertia with increasing heliocentric distance, which gave α = -1.66 $^{+1.04}/_{-1.06}$ and α = -0.78 $^{+0.78}/_{-1.78}$ for Ganymed and 2002 CE26, respectively. Whilst it was not possible to identify which spectral emissivity value was likely to be representative of Ganymed, it seemed that a value of 0.9 was suitable for 2002 CE26 based on the analysis for Betulia and other asteroids of a similar spectral type (e.g. Emery et al. 2014; Müller et al. 2017). Therefore, we consider the power-law fit obtained from a 4.6 μm spectral emissivity of 0.9 to be representative of 2002 CE26.

As a comparison, it was possible to analyse the mean thermal inertia values of Centaurs/TNOs given by Lellouch et al. (2013) in this framework. In particular, Lellouch et al. (2013) give the mean thermal inertia value of Centaurs/TNOs as 5 ± 1 J m^{-2} K^{-1} s$^{-1/2}$ for r_H = 8 to 25 AU (i.e. ~16.5 AU), 2.5 ± 0.5 J m^{-2} K^{-1} s$^{-1/2}$ for r_H = 25 to 41 AU (i.e. ~33 AU), and 2 ± 0.5 J m^{-2} K^{-1} s$^{-1/2}$ for r_H = 41 to 53 AU (i.e. ~47 AU). As shown in Figure 7, these measurements indicate a variation in thermal inertia with heliocentric distance that is similar to that of Ganymed and 2002 CE26, and a chi-squared fit of the power-law above gave Γ_0 = 65 $^{+215}/_{-55}$ J m^{-2} K^{-1} s$^{-1/2}$ and α = -0.92 $^{+0.38}/_{-0.46}$ (see Figure 8). The derived exponent value is consistent with the interpretation given by Lellouch et al. (2013) in that Centaurs/TNOs obey a $\Gamma \propto r_H^{-1}$ trend expected of icy surfaces.

3. DISCUSSION

3.1 Physical interpretation of the observed variation

The values of -2.22 $^{+0.68}/_{-0.66}$ and -1.46 $^{+0.86}/_{-1.22}$ measured for the exponent α of Ganymed and 2002 CE26, respectively, are more extreme than the expected exponent of -0.75 when considering the arguments discussed in Section 1.1. However, an exponent of -0.75 cannot be ruled out when considering the large uncertainty on the derived values and the influence of the spectral emissivity at 4.6 µm. Nevertheless, it does raise a question of what could cause a more extreme exponent than expected, and the answer to this question requires more in-depth consideration of the three material properties that combine to give thermal inertia: the thermal conductivity, specific heat capacity, and density. These three properties are discussed in more detail below.

The total thermal conductivity of a planetary regolith layer is comprised of the sum of three components: the solid, radiative, and gas thermal conductivity. The solid thermal conductivity arises from the transport of heat through the solid network of particles that form the regolith layer. From measurements of various meteorites in Opeil et al. (2010), the solid thermal conductivity of the bulk materials that form asteroids are approximately a linear function of temperature. However, for a porous material, the solid thermal conductivity can be orders of magnitude lower than the solid thermal conductivity of the bulk material because of the small contact areas between the particles that reduce the heat exchange efficiency (Gundlach & Blum 2012). The radiative thermal conductivity arises from the heat exchanged between particles by emitted and absorbed photons, which, as described above, is proportional to T^3. The gas thermal conductivity arises from the heat transport by conduction through the gas in the pores between particles, and is essentially zero for atmosphereless asteroidal surfaces. The processes behind the solid and radiative components of thermal conductivity in porous regolith are well understood, and theoretical models describing their magnitude have been validated by laboratory investigations (e.g. Gundlach & Blum 2012, 2013).

For instance, Gundlach & Blum (2013) have produced a semi-empirical relationship for calculating the thermal conductivity of a regolith layer, which is routinely applied to thermal inertia measurements in order to estimate the grain sizes of various planetary surfaces. In a simplified form, this relationship for the thermal conductivity, $k(T,r,\varphi)$, is given by

$$k\left(T,r,\phi\right)=3.79\times10^{-7}\times k_{\mathrm{solid}}\left(T\right)\left(\frac{T}{r}\right)^{1/3}e^{5.26\phi}+6.08\times10^{-7}\times\varepsilon T^3\frac{1-\phi}{\phi}r\,, \tag{4}$$

where r is the radius of the regolith grains, φ is the regolith grain packing fraction, $k_{\mathrm{solid}}(T)$ is the solid thermal conductivity of the bulk material, and ε is the bolometric emissivity. The solid thermal conductivity can have a constant value or vary with temperature depending on the type of materials considered. The overall thermal inertia value, $\Gamma(T,r,\varphi)$, is then given by

$$\Gamma\left(T,r,\phi\right)=\sqrt{k\left(T,r,\phi\right)\phi\rho_0 C_{\mathrm{P}}}\,, \tag{5}$$

where C_{P} is the specific heat capacity as before, and ρ_0 is the grain density of the regolith material (i.e. the overall density of the regolith layer is given by $\rho = \varphi\rho_0$). Typically, the sub-solar temperature, T_0, of a planetary body is used in equation (4), which can be calculated from

$$T_0 = \left[\frac{S_0 (1 - A_\mathrm{B})}{\eta \varepsilon \sigma r_\mathrm{H}^2} \right]^{1/4}, \tag{6}$$

where S_0 is the solar constant at 1 AU (i.e. 1367 W m^{-2}), A_B is the Bond albedo, and η is the NEATM beaming parameter (Harris 1998). It is possible to make a theoretical prediction of the functional form of the variation of thermal inertia with heliocentric distance by using equations (4), (5) and (6) with suitable values for the input parameters. For example, if an S-type asteroid has a thermal inertia of 270 J m^{-2} K^{-1} s$^{-1/2}$ at 1 AU then a suitable set of input parameters would include an average grain radius of 1 mm, a particle packing fraction of 0.3, a constant solid thermal conductivity of 2.18 W m^{-1} K^{-1}, a grain density of 3700 kg m^{-3}, a constant specific heat capacity of 860 J kg^{-1} K^{-1}, a Bond albedo of 0.1, a bolometric emissivity of 0.9, and, finally, a beaming parameter value of 1. The solid line in the left panel of Figure 9 gives the theoretical variation of thermal inertia with heliocentric distance for this example asteroid. Fitting the power-law of equation (3) to this theoretical prediction gives an exponent α of -0.74. This predicted value is close to the previously expected value of -0.75 because the second term on the right-hand side of equation (4) dominates the thermal conductivity calculation for low packing fractions. For higher packing fractions and/or smaller grain radii, the first term on the right-hand side of equation (4) would contribute more to the thermal conductivity calculation, and would therefore raise the value of the exponent α.

The variation of specific heat capacity with temperature for asteroidal materials at relevant temperatures has not been well studied. The US Geological Survey records thermodynamic properties, including specific heat capacity, for a wide range of minerals (e.g. Robie & Hemingway 1995). However, these measurements are generally at room temperature and pressure, or higher, and do not include the complex mixtures of minerals and structures expected on asteroid surfaces. The Debye phonon model (Debye 1912) plus electron specific contribution predicts the molar heat capacity of monatomic solids that provides a good match to the measurements. At low temperatures, the molar heat capacity at constant volume, C_V, rises as T^3 for insulators and T for conductors. At high temperatures, C_V asymptotically approaches a value of ~$3k_\mathrm{B}N_\mathrm{A}$, i.e. the Dulong and Petit limit, where k_B and N_A are the Boltzmann and Avogadro constants, respectively (Dulong & Petit 1819). The transition region between these two regimes lies at temperatures of a few hundred Kelvin. Assuming that more complex mineral mixtures behave in a similar way, the influence of the temperature-dependence of specific heat capacity on thermal inertia will depend critically on which regime applies to the asteroid surface temperatures at different heliocentric distances.

Fortunately, Macke et al. (2016) have recently made measurements of the specific heat capacity of ordinary chondrite meteorites, which are representative of S-type asteroidal material, over the temperature range of 5 to 350 K. They fit their specific heat capacity measurements, $C_\mathrm{P}(T)$, with the function

$$C_\mathrm{P}(T) = A + BT + CT^{-2} + DT^{-1/2} \tag{7}$$

where A, B, C, and D are coefficients describing the curves that best fit their data. Averaging the results presented in Table 1 of Macke et al. (2016) gives $A = 1406.7$, $B = 0.33026$, $C = 1.6872 \times 10^6$, and $D = -1.3580 \times 10^4$. Using this functional form of $C_\mathrm{P}(T)$ in equation (5) allows the temperature-dependence of specific heat capacity to be included in the theoretical variation of thermal inertia

with heliocentric distance. This is shown by the dashed line in the left panel of Figure 9 for the same example asteroid discussed earlier. This prediction also assumes that equation (7) and its four coefficients still apply to temperatures greater than 350 K. As shown, including the temperature-dependence of specific heat capacity, in addition to that of thermal conductivity, produces a steeper trend of thermal inertia versus heliocentric distance, which is characterised by a lower value of -0.92 for the exponent α. Therefore, the temperature-dependence of specific heat capacity does contribute slightly to more extreme values of the exponent α.

The overall density of the regolith layer is dictated by the grain density of the material of which it is comprised and the particle packing fraction. Both of these properties have a negligible variation with temperature. However, the packing fraction of the regolith layer is influenced by other processes related to the asteroid environment. For example, these processes include impact cratering, slope failures and collapses, seismic shaking, particle segregation, tidal and rotational forces, and others [e.g. see review by Murdoch et al. (2015)]. Such processes typically act on timescales much longer than the orbital period, and are unlikely to contribute to the thermal inertia variation seen here. However, one possibility is that the packing fraction of the surface layer is sensitive to variations in solar radiation pressure and solar wind intensity, which both decrease with increasing distance from the Sun. It is known that solar radiation pressure has a strong influence on the trajectory of particles ejected from the surface of an asteroid (e.g. Scheeres 1999) but it is unclear what influence it has on particles resting on the surface (Scheeres et al. 2010). In fact, solar radiation pressure may not matter at all if cohesive forces are present within the asteroid, since these forces would dominate the surface environment. For instance, the minimum cohesive strength of 2002 CE26 can be estimated by using the Druger-Prager failure criterion (Holsapple 2007) with the radar-derived shape, spin rate, and bulk density. As shown in Figure 10, it is quite likely that 2002 CE26 has some degree of cohesion to prevent rotational breakup because of its rather low bulk density for its spin rate. Assuming an angle of friction consistent with lunar regolith of 40° (Mitchell et al. 1974) gives a minimum cohesive strength of 70 $^{+20}/_{-55}$ Pa, which is comparable to that of 64 $^{+12}/_{-20}$ Pa determined for 1950 DA by Rozitis et al. (2014). Therefore, it seems unlikely that solar radiation pressure could influence the packing fraction of the surface layer. The solar wind, in addition to direct sunlight, is thought to cause electrostatic dust levitation (Hughes, Colwell & DeWolfe 2008), which is one possible way to remove particles from the surface. This process could reduce the packing fraction of the surface, but, again, it would be limited by any cohesion present.

Considering the above arguments, and using the latest models to describe heat transfer within asteroidal regoliths, indicates that the minimum theoretical value the exponent α could take is around -0.9. However, this lower limit on the exponent α is obtained for thermal properties that are constant with depth and vary with temperature only. Harris & Drube (2016) have recently identified a trend of increasing asteroid thermal inertia with increasing rotation period, which they interpret as asteroids having a surface layer that rapidly increases in thermal inertia with depth within the top 10 cm. This is much like the lunar surface that was studied *in situ* near the Apollo landing sites (Keihm et al. 1973; Keihm & Langseth 1973). As the asteroid rotation period is increased, it also increases the thermal skin depth, which is a measure of how deep a thermal wave penetrates below the surface and is typically a few centimetres in length. For reference purposes, the thermal skin depth L is given by

$$L = \frac{\Gamma}{\rho C_{\mathrm{P}}} \sqrt{\frac{P}{2\pi}} ,$$

(8)

where P is the asteroid rotation period. An increased thermal skin depth enables the thermal wave to sample the higher thermal inertia material below, and increases the 'effective' thermal inertia seen by thermal-infrared observations. This would then create the observed trend of increasing asteroid thermal inertia with increasing rotation period.

A similar situation would arise in the case of temperature-dependent thermal inertia as discussed here, i.e. a hotter surface would increase its thermal inertia value which then increases its thermal skin depth. The right panel of Figure 9 demonstrates the variation in thermal skin depth with heliocentric distance for the example asteroid discussed earlier. Again, an increased thermal skin depth enables the thermal wave to sample the higher thermal inertia material below, which then enhances the increase in 'effective' thermal inertia caused by temperature-dependent effects. The two effects of temperature and depth dependence combined would result in values of the exponent α that are more extreme than initially expected, and could explain the values measured for Ganymed and 2002 CE26. For a full explanation, an increase in thermal inertia with depth can be achieved by increased packing fraction and/or increased grain size, and would require sophisticated modelling of the heat transfer within asteroidal regoliths to disentangle. This is beyond the scope of this work, but additional and more accurate measurements of the exponent α for more asteroids would place useful constraints on any future modelling efforts.

Finally, the uncertainties in the results do not allow us to determine whether the difference in the exponent α for Ganymed and 2002 CE26 is significant. It is possible that different classes of asteroid will exhibit different exponents as a result of their surface compositions and structures. Further observations of objects with higher precision are required to determine if this is the case.

3.2 Implications for asteroids

An important implication of thermal inertia varying with heliocentric distance is in the interpretation of the apparent trend of decreasing thermal inertia with increasing asteroid size, i.e. see left panel of Figure 11. This trend contains both near-Earth asteroids, which primarily represent asteroids smaller than 10 km in size, and main-belt asteroids, which primarily represent asteroids much bigger than 10 km in size. One interpretation of this apparent thermal inertia versus size trend is that it is related to the relative ages of those asteroids. Larger asteroids are older than smaller asteroids, and therefore their surfaces were exposed to regolith-producing processes for longer. For example, processes like impact gardening (Housen et al. 1979; Hörz & Cintala 1997) and thermal fracturing (Delbo et al. 2014) require time to grind the regolith grains down to smaller sizes. Another interpretation is that larger asteroids have higher surface gravities, and are therefore more able to hold on to fine regolith grains (Gundlach & Blum 2013). However, this trend does not take into account the heliocentric distance at which the thermal inertia of each asteroid was measured. In particular, the near-Earth asteroids generally had their thermal inertia values measured at heliocentric distances of less than 2 AU, and the main-belt asteroids were measured at heliocentric distances greater than 2 AU. Therefore, the variation of thermal inertia with heliocentric distance could contribute significantly to this apparent trend.

To describe the apparent thermal inertia versus size trend, Delbo et al. (2007) introduced a power-law of the form

$$\Gamma = d_0 D^\xi,$$ (9)

where d_0 is the thermal inertia of a 1-km sized asteroid, D is the asteroid diameter in km, and ξ is an exponent describing the size trend. A linear regression in log-log space to the thermal inertia values of 14 asteroids measured at that time gave a best fit of d_0 = 300 ± 47 J m^{-2} K^{-1} s$^{-1/2}$ and ξ = -0.47 ± 0.04. A more up to date calculation using the 40 asteroids displayed in Figure 14 gives a best fit of d_0 = 280 ± 62 J m^{-2} K^{-1} s$^{-1/2}$ and ξ = -0.37 ± 0.05. As summarised in Table 5, adjusting the thermal inertia of each asteroid to a common heliocentric distance of 1 AU using equation (3) with various values of the exponent α changes the result of this linear regression. In particular, the exponent ξ increases for decreasing exponent α such that the trend of thermal inertia versus size becomes less and less apparent. For a surprisingly reasonable value of the exponent α, i.e. α = -2.7, the thermal inertia versus size trend disappears, i.e. ξ = 0, and places a lower limit on its value (see right panel of Figure 11). If the exponent α was any less than this value then the asteroid thermal inertia would start increasing with increasing asteroid size. Utilising the values of the exponent α measured for Ganymed and 2002 CE26, i.e. α = -2.22 to -1.46, indicates that the exponent ξ could lie somewhere between -0.17 and -0.07. This would imply that the surfaces of small and large asteroids are much more similar than previously thought. Similar surfaces could arise if the regolith production processes are independent of asteroid size, and/or take place on a timescale much shorter than the typical dynamical lifetime of a small asteroid.

3.3 Implications for the Yarkovsky effect

Another important implication of thermal inertia varying with heliocentric distance is in the calculation of Yarkovsky orbital drift for a near-Earth asteroid. At present, most Yarkovsky models assume constant thermal properties in the calculation of the net photon recoil force acting on an asteroid as it orbits the Sun [e.g. see Rozitis & Green (2012) and Vokrouhlický et al. (2015) for a review]. To evaluate the potential impact on Yarkovsky orbital drift calculations, we performed a small parameter study on the predicted orbital drift of five near-Earth asteroids, which were 2002 CE26 and the four asteroids we have investigated previously in other work, i.e. (1620) Geographos (Rozitis & Green 2014), (1862) Apollo (Rozitis et al. 2013), (29075) 1950 DA (Rozitis et al. 2014), and (101955) Bennu (Chesley et al. 2014; Emery et al. 2014). As summarised in Table 6, they have a range of orbital eccentricities, and a range of thermal inertia values measured at different heliocentric distances.

The Yarkovsky effect acting on each asteroid was determined by computing the total recoil force of photons thermally emitted from the asteroid surface. The ATPM described in Section 2.1 was used to calculate the needed surface temperatures as a function of the asteroid thermal inertia. The photon recoil force was then averaged over both the asteroid rotation and elliptical orbit in order to give the overall Yarkovsky orbital drift [i.e. see Rozitis & Green (2012, 2013) for more details]. In the case of thermal inertia unchanging with heliocentric distance, the thermal inertia was simply kept constant around the asteroid orbit within the ATPM. For thermal inertia varying with heliocentric distance, the thermal inertia was varied according to equation (3) as the asteroids moved around their elliptical orbits within the ATPM. The Yarkovsky orbital drift for each asteroid

was then evaluated as a function of the exponent α by setting their initial thermal inertia values at the heliocentric distances at which their measurements were made. All of the asteroids were assumed to have a moderate surface roughness fraction of 0.5. The size, shape, rotation state, and bulk density of each asteroid were also set to the same quantities as those used/determined in the previous works mentioned above. Figure 12 shows the Yarkovsky orbital drift as a function of the exponent α for the five asteroids considered, and Table 6 also summarises the results.

As shown in Figure 12 and Table 6, 1950 DA and 2002 CE26 showed a significant variation with the exponent α whilst the other asteroids did not. For these two asteroids, the rate of Yarkovsky orbital drift increased by a few tens of per cent as the exponent α decreased, which indicated that the overall Yarkovsky force acting on them increased by the same amount as the exponent α decreased. Therefore, the bulk density of these two asteroids would be underestimated in model-to-measurement comparisons of Yarkovsky orbital drift if the variation of thermal inertia with heliocentric distance was not taken into account. This would be important for 1950 DA because its low bulk density, which was determined from model-to-measurement comparisons of Yarkovsky orbital drift, indicated the need of cohesive forces to prevent its rotational breakup (Rozitis et al. 2014). In particular, an increased bulk density of 1950 DA would lower the minimum amount of cohesion needed for rotational stability. It was interesting that the three other asteroids investigated did not show a strong relationship of their Yarkovsky orbital drift with the exponent α. It appears that asteroids with more circular orbits, and/or with particular pole orientations with respect to their orbits, were less sensitive to the effects of thermal inertia varying with heliocentric distance. Therefore, in future work, each asteroid to be investigated for Yarkovsky orbital drift should be assessed for sensitivity to thermal inertia varying with heliocentric distance on a case by case basis.

4. SUMMARY AND CONCLUSIONS

In summary, the thermal inertia value of an asteroid is expected to vary with heliocentric distance because of the temperature-dependence of thermal conductivity and specific heat capacity. In order to detect a change in thermal inertia, large near-Earth asteroids on highly eccentric orbits are required with well-defined shape models and multiple thermal-infrared datasets. A search through the appropriate databases identified that the asteroids Ganymed and 2002 CE26 were suitable candidates for detecting a variation in thermal inertia with heliocentric distance. The search also identified asteroid Betulia as a suitable control for testing constant thermal inertia at constant heliocentric distance. All three asteroids had been observed by NEOWISE and its reactivated mission on multiple occasions.

Thermophysical modelling of the NEOWISE data for Ganymed and 2002 CE26 confirmed that their thermal inertia values did vary with heliocentric distance, although the degree of variation observed depended on the spectral emissivity assumed in the modelling. For an assumed 4.6 μm spectral emissivity of 0.9, the thermal inertia variations for Ganymed and 2002 CE26 can be described by $\Gamma = (500\ ^{+400}/_{-255})r_H{}^\wedge(-2.22\ ^{+0.68}/_{-0.66})$ and $\Gamma = (255\ ^{+165}/_{-105})r_H{}^\wedge(-1.46\ ^{+0.86}/_{-1.22})$ J m^{-2} K^{-1} s$^{-1/2}$, respectively. Decreasing the 4.6 μm spectral emissivity reduces the degree of variation observed for both asteroids. The thermal inertia value of Betulia (i.e. ~200 J m^{-2} K^{-1} s$^{-1/2}$) was also confirmed not to change when it was observed at the same heliocentric distance on three separate occasions. Furthermore, a comparative analysis of the thermal inertia values reported by Lellouch et al. (2013) for Centaurs/TNOs gave a similar heliocentric distance variation of $\Gamma = (65\ ^{+215}/_{-55})r_H{}^\wedge(-0.92\ ^{+0.38}/_{-0.46})$ J m^{-2} K^{-1} s$^{-1/2}$.

Depending on the spectral emissivity, the exponents describing the heliocentric distance variation observed for Ganymed and 2002 CE26 were potentially more extreme than currently predicted by theoretical models of heat transfer within asteroidal regoliths (i.e. about -0.9). This could indicate that Ganymed and 2002 CE26 have, in addition to thermal properties that vary with temperature, a surface layer that has a rapidly increasing thermal inertia with depth. This is consistent with the previously observed trend of increasing asteroid thermal inertia with increasing rotation period and its explanation given by Harris & Drube (2016). It is not likely to be caused by a variation in density or packing fraction with heliocentric distance because the presence of any cohesive forces would dominate over solar radiation pressure and solar wind. For instance, the minimum cohesive strength of 2002 CE26 was determined to be $70\ ^{+20}/_{-55}$ Pa.

The variation of thermal inertia with heliocentric distance has important implications for asteroids in general. For instance, taking into account this variation reduces the trend of decreasing thermal inertia with increasing asteroid size previously reported by Delbo et al. (2007). In particular, a heliocentric distance variation exponent of -2.7 causes the size trend to disappear, which places a lower limit on its value. A reduced size trend would indicate that the surfaces of small and large asteroids are much more similar than previously thought, and suggests that regolith production processes are independent of size and/or take place on timescales much shorter than the typical dynamical lifetime of a small asteroid.

The variation of thermal inertia with heliocentric distance also has important implications for modelling the Yarkovsky effect. In particular, it was found for some near-Earth asteroids that their modelled rates of Yarkovsky orbital drift were increased by a few tens of per cent when their

thermal inertia values were allowed to vary around their orbits. However, in contrast, it was also found for some asteroids that their predictions were relatively insensitive to varying thermal inertia. Therefore, each asteroid to be investigated for Yarkovsky orbital drift should be assessed for sensitivity to thermal inertia varying with heliocentric distance on a case by case basis.

In conclusion, asteroids on eccentric orbits do appear to have thermal inertia values that vary with heliocentric distance. Therefore, thermophysical models of these asteroids must consider changes in thermal inertia value if there are large variations in heliocentric distance within the thermal-infrared observations used for modelling. Constraining the variation of thermal inertia with heliocentric distance to a high degree has the potential to provide insights into the asteroid sub-surface structure within the top 10 cm. In particular, the upcoming asteroid sample return missions OSIRIS-REx (Lauretta et al. 2015) and Hayabusa 2 (Okada et al. 2012) both have thermal-infrared instruments onboard to aid sample site selection, and therefore will be capable of investigating the variation of thermal inertia with heliocentric distance *in situ* at their target asteroids.

ACKNOWLEDGEMENTS

REFERENCES

Alí-Lagoa V., de Léon J., Licandro J., Delbo M., Campins H., Pinilla-Alonso N., Kelley M. S., 2013, A&A, 554, A71
Balridge A. M., Hook S. J., Grove C. I., Rivera G., 2009, Remote Sens. Environ., 113, 711
Bowell E., Hapke B., Domingue D., Lumme K., Peltoniemi J., Harris A. W., 1989, in Binzel R. P., Gehrels T., Matthews M. S., eds, Asteroids II. University of Arizona Press, Tucson, p. 524
Bus S. J., Binzel R. P., 2002, Icarus, 158, 106
Busch M. W. et al., 2007, Icarus, 190, 608
Chesley S. R. et al., 2014, Icarus, 235, 5
Cruikshank D., van Cleve J., 2004, Spitzer Proposal ID #88
Davidsson B. J. R. et al., 2015, Icarus, 252, 1
Debye P., 1912, Ann. Phys., 344, 789
Decin L., Morris P. W., Appleton P. N., Charmandaris V., Armus L., Houck J. R., 2004, ApJS, 154, 408
Delbo M., dell'Oro A., Harris A. W., Mottola S., Mueller M., 2007, Icarus, 190, 236
Delbo M. et al., 2014, Nature, 508, 233
Delbo M., Mueller M., Emery J. P., Rozitis B., Capria M. T., 2015, in Michel P., DeMeo F. E., Bottke W. F., eds, Asteroids IV. University of Arizona Press, Tucson, p. 107
Emery J. P. et al., 2014, Icarus, 234, 17
Fowler J. W., Chillemi J. R., 1992, in Tedesco E. F., Veeder J. W., Fowler J. W., Chillemi J. R., eds, The IRAS Minor Planet Survey. Philips Laboratory, Hanscom AF Base, p. 17

Gueymard C. A., 2004, Solar Energy, 76, 423

Gundlach B., Blum J., 2012, Icarus, 219, 618

Gundlach B., Blum J., 2013, Icarus, 223, 479

Hahn G. et al., 1989, Icarus, 78, 363

Hanus J., Delbo M., Durech J., Ali-Lagoa V., 2015, Icarus, 256, 101

Hanus J. et al., 2016, A&A, 592, A34

Harris A. W., 1998, Icarus, 131, 291

Harris A. W., Drube L., 2016, ApJ, 832, 127

Harris A. W., Mueller M., Delbo M., Bus S. J., 2005, Icarus, 179, 95

Holsapple K. A., 2007, Icarus, 187, 500

Hörz F., Cintala M., 1997, M&PS, 32, 179

Houck J. R. et al., 2004, ApJS, 154, 18

Housen K. R., Wilkening L. L., Chapman C. R., Greenberg R., 1979, Icarus, 39, 317

Hughes A. L. H., Colwell J. E., DeWolfe A. W., 2008, Icarus, 195, 630

Jarrett T. H. et al., 2011, ApJ, 735, 112

Kaasalainen M. et al., 2004, Icarus, 167, 178

Keihm S. J., Langseth M. G., 1973, Proc. Lunar Sci. Conf., 4, 2503

Keihm S. J., Peters K., Langseth M. G., Chute J. L., 1973, Earth Planet. Sci. Lett., 19, 337

Kieffer H. H., 2013, J. Geophys. Res., 118, 451

Lauretta D. S. et al., 2015, M&PS, 50, 834

Lebofsky L. A., Veeder G. J., Lebofsky M. J., Matson D. L., 1978, Icarus, 35, 336

Lebouteiller V., Barry D. J., Spoon H. W. W., Bernard-Salas J., Sloan G. C., Houck J. R., Weedman D. W., 2011,
        ApJS, 196, 8

Lellouch E. et al., 2013, A&A, 557, A60

Lim L. F., McConnochie T. H., Bell J. F., Hayward T. L., 2005, Icarus, 173, 385

Lowry S., Duddy S. R., Rozitis B., Green S. F., Fitzsimmons A., Snodgrass C., Hsieh H. H., Hainaut O., 2012, A&A,
        548, A12

Macke R. J., Opeil C. P., Consolmagno G. J., Britt D. T., 2016, in 47th Lunar and Planetary Science Conference,
        LPI Contr. 1903, 1221

Magri C., Ostro S. J., Scheeres D. J., Nolan M. C., Giorgini J. D., Benner L. A. M., Margot J.-L., 2007, Icarus, 186,
        152

Mainzer A. et al., 2011, ApJ, 743, 156

Marsset M. et al., 2017, A&A, 604, A64

Mitchell J. K., Houston W. N., Carrier W. D., Costes N. C., 1974, Space Sciences Laboratory Series, 15, 72

Müller T. G. et al., 2017, A&A, 599, A103

Müller T. G., Hasegawa S., Usui F., 2014, PASJ, 66, 5217

Murdoch N., Sánchez P., Schwartz S. R., Miyamoto H., 2015, in Michel P., DeMeo F. E., Bottke W. F., eds,
        Asteroids IV. University of Arizona Press, Tucson, p. 767

Nugent C. R., 2013, PhD thesis, Univ. California

Nugent C. R. et al., 2015, ApJ, 814, 117

Nugent C. R. et al., 2016, AJ, 152, 63

Okada T. et al., 2012, in 43rd Lunar and Planetary Science Conference, LPI Contr. 1659, 1498

Opeil C. P., Consolmagno G. J., Britt D. T., 2010, Icarus, 208, 449

Petit A.-T., Dulong P.-L., 1819, Ann. Chim. Phys., 10, 395

Pettengill G. H., Ostro S. J., Shapiro I. I., Marsden B. G., Campbell D. B., 1979, Icarus, 40, 350

Rivkin A. S., Ellen S. H., Emery J. P., Sunshine J., 2018, Icarus, 304, 74

Robie R. A., Hemingway B. S., 1995, U.S. Geol. Survey Bull., 2131, 461

Rozitis B., 2017, MNRAS, 464, 915

Rozitis B., Green S. F., 2011, MNRAS, 415, 2042

Rozitis B., Green S. F., 2012, MNRAS, 423, 367

Rozitis B., Green S. F., 2013, MNRAS, 433, 603

Rozitis B., Green S. F., 2014, A&A, 568, A43

Rozitis B., Duddy S. R., Green S. F., Lowry S. C., 2013, A&A, 555, A20

Rozitis B., Maclennan E., Emery J. P., 2014, Nature, 512, 174

Scheeres D. J., 1999, Celest. Mech. Dyn. A., 73, 339

Scheeres D. J., Hartzell C. M., Sánchez P., Swift M., 2010, Icarus, 210, 968

Shepard M. K. et al., 2006, Icarus, 184, 198

Snyder W., Wan Z., Zhang Y., Feng Y.-Z., 1997, Remote Sens. Environ., 60, 101

Tedesco E. F., 1986, in Matson D. L., ed., Infrared Astronomical Satellite Asteroid and Comet Survey: Preprint Version No. 1. Jet Propulsion Laboratory Publication D-3698, pp. 9:1-9:42

Tedesco E., Drummond J., Candy M., Birch P., Nikoloff I., Zellner B., 1978, Icarus, 35, 344

Tedesco E. F., Noah P. V., Noah M., Price S. D., 2002, AJ, 123, 1056

Usui F. et al., 2011, PASJ, 63, 1117

Wan Z., Ng D., Dozier J., 1994, Adv. Space Res., 14, 91

Werner M. W. et al., 2004, ApJS, 154, 1

Werner R. A., Scheeres D. J., 1997, Celest. Mech. Dyn. A., 65, 313

Williams G. V., 2012, PhD thesis, Open Univ.

Wolters S. D., Green S. F., McBride N., Davies J. K., 2008, Icarus, 193, 535

Wolters S. D., Rozitis B., Duddy S. R., Lowry S. C., Green S. F., Snodgrass C., Hainaut O. R., Weissman P., 2011, MNRAS, 418, 1246

Wright E. L. et al., 2010, AJ, 140, 1868

Vasavada A. R., Paige D. A., Wood S. E., 1999, Icarus, 141, 179

Veeder G. J., Hanner M. S., Matson D. L., Tedesco E. F., Lebofsky L. A., Tokunaga A. T., 1989, AJ, 97, 1211

Vokrouhlický D., Bottke W. F., Chesley S. R., Scheeres D. J., Statler T. S., 2015, in Michel P., DeMeo F. E., Bottke W. F., eds, Asteroids IV. University of Arizona Press, Tucson, p. 509

APPENDIX A: REFLECTED SOLAR RADIATION AT SHORT THERMAL WAVELENGTHS

Similar to Ali-Lagoa et al. (2013), the following methodology was used to determine the amount of reflected solar radiation in the W2 channel observations of Ganymed. Firstly, the asteroid visible magnitude, V, at the time of the observations was calculated by using the IAU phase curve correction (Bowell et al. 1989) with the geometries given in Table 2, and with suitable values for the asteroid absolute magnitude, H, and phase slope, G. Fortunately, the visible phase curve of Ganymed has been well studied due to its relatively large size. In particular, reported H and G values for Ganymed include 9.42 and 0.31 by Tedesco (1986), 9.50 ± 0.01 and 0.33 ± 0.02 by Hahn et al. (1989), 9.52 ± 0.01 and 0.29 ± 0.01 by Williams (2012), and 9.45 and 0.30 currently given by the Minor Planet Center. These measured values were combined by taking their mean value and standard deviation to give H and G as 9.47 ± 0.05 and 0.31 ± 0.02, respectively. Using these mean values, Ganymed's visible magnitude (i.e. the light-curve average value) was then calculated to be 15.94 ± 0.05, 15.45 ± 0.05, 14.88 ± 0.06 and 13.24 ± 0.06 during the January 2010, June 2010, February 2015, and July 2015 sets of NEOWISE observations, respectively.

Secondly, Ganymed's visible magnitude was compared with that of the Sun, V_{SUN} (i.e. -26.74), to determine the amount of reflected solar radiation. In particular, Ganymed's reflected flux is a factor of $10^{\frac{V-V_{\mathrm{SUN}}}{2.5}}$ less than that of the solar flux at 1 AU at any given wavelength when assuming that all wavelengths are reflected equally. However, asteroids have different reflectances at different wavelengths. To take this into account, the scaled solar flux must also be multiplied by the ratio of Ganymed's geometric albedo at a particular wavelength to its visible geometric albedo, p_λ/p_{V}. Therefore, the amount of reflected solar radiation at wavelength λ, $F_{\mathrm{REF},\lambda}$, could be calculated from Ganymed's visible magnitude at the time of the observations by using

$$F_{\mathrm{REF},\lambda} = \frac{p_\lambda}{p_{\mathrm{V}}} S_\lambda 10^{\frac{V_{\mathrm{SUN}}-V}{2.5}} , \qquad (A1)$$

where S_λ is the monochromatic solar flux at 1 AU. For the W2 channel, the corresponding solar flux at a wavelength of 4.6 μm was 4.594 W m^{-2} μm^{-1} (Gueymard 2004).

In order to use equation (A1), knowledge of Ganymed's $p_{4.6\mu m}/p_{\mathrm{V}}$ reflectance ratio was required. In previous studies, Mainzer et al. (2011) assumed that the reflectances in the W1 and W2 channels were equal, and determined the ratio of the infrared geometric albedo to the visible geometric albedo, i.e. $p_{\mathrm{IR}}/p_{\mathrm{V}}$, for Ganymed to be between 1.38 and 1.47 from NEATM modelling of the January and June 2010 NEOWISE observations. However, near-infrared spectral observations obtained by Rivkin et al. (2018) show that the reflectances in the W1 and W2 channels cannot be equal, and they find a somewhat lower reflectance ratio of 1.25 to 1.30. Since the near-infrared spectral observations provide a more direct comparison of the asteroid reflectance at the different wavelengths, we decided to re-evaluate the $p_{4.6\mu m}/p_{\mathrm{V}}$ reflectance ratio using the NEOWISE data.

For this re-evaluation, we performed a bootstrap analysis on the January and June 2010 NEOWISE observations using NEATM (Harris 1998). In this analysis, the NEATM was fitted to the W3 and W4 channel data only, which allowed predictions of the W2 channel thermal flux to be made using the fitted NEATM parameters. The W1 channel data was ignored to provide unbiased measurements of Ganymed's $p_{4.6\mu m}/p_{\mathrm{V}}$ reflectance ratio. In each bootstrap trial, the W3 and W4

channel data, and also Ganymed's H and G values, were randomly selected from Gaussian distributions centred on the measured values with widths equal to the measurement uncertainties. One thousand trials were performed to determine statistical uncertainties of the fitted NEATM parameters, namely D, p_V, and η (i.e. the beaming parameter), and the uncertainty of the predicted W2 channel thermal flux, $F_{TH,4.6\mu m}$. For the January 2010 observations, this analysis determined D = 34.4 ± 0.3 km, p_V = 0.24 ± 0.01, and η = 0.88 ± 0.02, which compares well to that of D = 35.3 ± 0.5 km, p_V = 0.24 ± 0.04, and η = 0.84 ± 0.03 determined by Mainzer et al. (2011). The predicted W2 channel thermal flux including the appropriate colour correction was $F_{TH,4.6\mu m}$ = 1.61 ± 0.05 ×10^{-17} W m^{-2} μm^{-1} when assuming a spectral emissivity of 0.9. Likewise, for the June 2010 observations, this analysis determined D = 36.4 ± 0.3 km, p_V = 0.22 ± 0.01, and η = 0.94 ± 0.01, which compares well to the Mainzer et al. (2011) values of D = 37.7 ± 0.4 km, p_V = 0.22 ± 0.05, and η = 0.96 ± 0.04. In this case, the predicted W2 channel thermal flux was $F_{TH,4.6\mu m}$ = 4.65 ± 0.13 ×10^{-17} W m^{-2} μm^{-1}. The smaller uncertainties in our analysis result from adopting tighter constraints on Ganymed's H and G values.

In comparison, the total observed flux in the W2 channel, i.e. $F_{TOTAL,4.6\mu m}$ = $F_{TH,4.6\mu m}$ + $F_{REF,4.6\mu m}$, during the January and June 2010 NEOWISE observations was 6.51 ± 0.45 and 11.68 ± 0.29 ×10^{-17} W m^{-2} μm^{-1} (i.e. the mean value and standard error), respectively. Subtracting the thermal fluxes calculated above gives the corresponding reflected flux in the W2 channel as 4.90 ± 0.45 and 7.03 ± 0.32 ×10^{-17} W m^{-2} μm^{-1}. By assuming a $p_{4.6\mu m}/p_V$ reflectance ratio of 1, and using the predicted visible magnitudes given above, equation (A1) gives a nominal predicted reflected flux in the W2 channel as 3.90 ± 0.20 and 6.11 ± 0.30 ×10^{-17} W m^{-2} μm^{-1}. Therefore, by comparing the reflected flux determined from the measurements with that nominally predicted gives the $p_{4.6\mu m}/p_V$ reflectance ratios of 1.26 ± 0.13 and 1.15 ± 0.08 for the January and June 2010 NEOWISE observations, respectively. These are somewhat lower than those determined by Mainzer et al. (2011) but are in good agreement with that found by Rivkin et al. (2018).

Combining the three measurements of 1.26 ± 0.13, 1.15 ± 0.08, and 1.28 ± 0.05 from the NEOWISE and near-infrared spectral observations gives an overall value of 1.23 ± 0.11 for the $p_{4.6\mu m}/p_V$ reflectance ratio of Ganymed. Therefore, using this value with the predicted visible magnitudes in equation (A1) gives the reflected flux in the W2 channel as 1.27 ± 0.13 and 5.77 ± 0.58 ×10^{-16} W m^{-2} μm^{-1} for the February and July 2015 reactivated NEOWISE observations, respectively. Since the total observed flux in the W2 channel was 2.22 ± 0.08 and 32.31 ± 0.58 ×10^{-16} W m^{-2} μm^{-1} (again, mean value and standard error), this then implies that the thermal component contribution was 42.6 ± 6.2 and 82.2 ± 1.8 per cent, respectively. Supplementary Table S5 summarises the results of this analysis when repeated for different values of the spectral emissivity at 4.6 μm.

APPENDIX B: ROTATIONALLY AVERAGED FLUX FITTING VERIFICATION

To determine whether fitting rotationally averaged flux produced reliable thermal inertia measurements, the methodology described in Sections 2.3 and 2.4.3 was tested on the NEOWISE data of asteroid 1950 DA previously studied in Rozitis et al. (2014). The NEOWISE observations were taken on 12-13 July 2010 when 1950 DA was at a heliocentric distance of 1.7 AU, a geocentric distance of 1.4 AU, and had a phase angle of 36° (Mainzer et al. 2011). The acquired observations uniformly sampled the thermal light-curve of 1950 DA with 14 flux data points from the W3 channel. In Rozitis et al. (2014), the ATPM was fitted to these data using the retrograde radar-derived shape model of 1950 DA (Busch et al. 2007) with the thermal inertia, roughness fraction, and rotation phase left as free parameters in the model fitting. The diameter was varied between its radar constrained range of 1.17 to 1.43 km, which allowed the thermal inertia of 1950 DA to be constrained as $24^{+20}/_{-14}$ J m^{-2} K^{-1} s$^{-1/2}$ with a model fit reduced-χ^2 of 1.06. As shown by the solid line in Supplementary Figure S4, the ATPM produced a good match to the observed thermal light-curve of 1950 DA when using its radar-derived shape model. In the alternative fitting method tested here, the model emitted flux was rotationally averaged, and the standard deviation of the rotational variation in flux was added in quadrature to the measured flux uncertainties. The free parameters in this fitting procedure were just the thermal inertia and surface roughness, and the thermal inertia of 1950 DA was constrained to be $26^{+18}/_{-16}$ J m^{-2} K^{-1} s$^{-1/2}$ with a model fit reduced-χ^2 of 1.24. This fit is shown by the dashed line in Supplementary Figure S4, and confirms that fitting rotationally averaged flux does produce reliable thermal inertia measurements for spheroidal shaped asteroids.
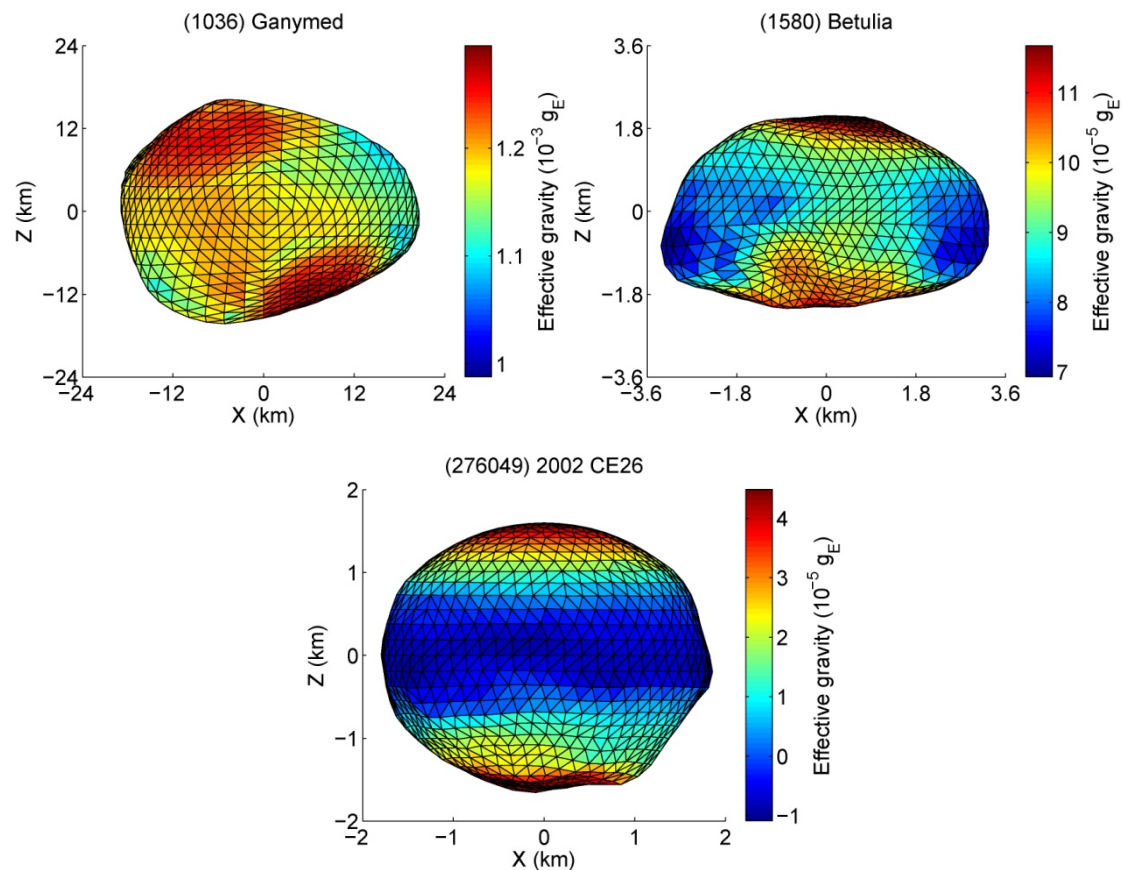
Figure 1: Shape models and effective surface gravity of the three near-Earth asteroids studied. The shape model of (1036) Ganymed was produced by light-curve inversion by Hanus et al. (2015), and the shape models of (1580) Betulia and (276049) 2002 CE26 were produced by radar imaging by Magri et al. (2007) and Shedpard et al. (2006), respectively. The effective surface gravity for each asteroid was computed by using a polyhedral gravity field model that also took into account rotational centripetal acceleration (Werner & Scheeres 1997; Rozitis et al. 2014). For the effective surface gravity calculations, bulk densities of 2000, 1500, and 900 kg m^{-3} were assumed for Ganymed, Betulia, and 2002 CE26, respectively. The facets of the Ganymed shape model were also recast to a uniform distribution in order to aid this calculation.
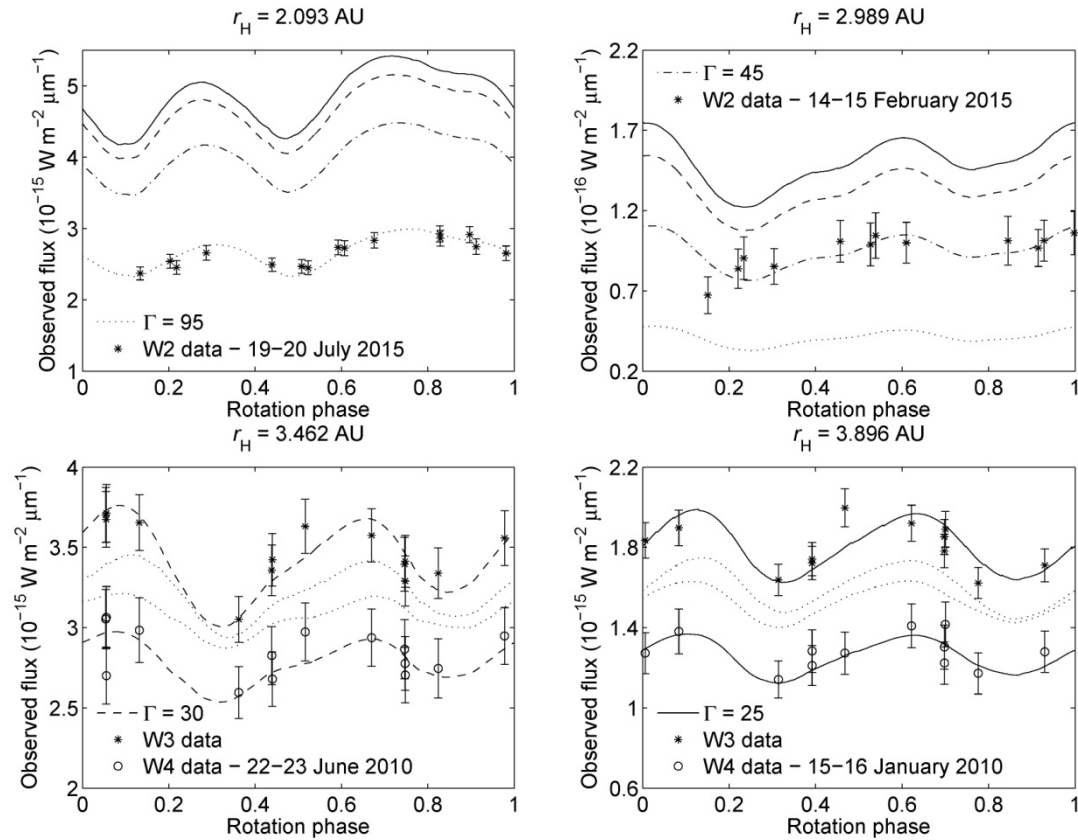
Figure 2: Thermal-infrared fits to the four different datasets of (1036) Ganymed. The top two panels give the fluxes measured by the reactivated NEOWISE mission in the W2 channel after reflected solar radiation was removed. The bottom two panels give the fluxes measured by the main NEOWISE mission in the W3 and W4 channels where no subtraction of reflected solar radiation was required. The error bars represent the 1-σ uncertainties on the measured flux data points. The lines represent the ATPM fits to each dataset where the different line styles correspond to the different thermal inertia values indicated in the figure legends. The W4 channel data points and the corresponding ATPM predictions in the bottom right panel have been shifted down by 0.4×10^{-15} W m^{-2} µm^{-1} to avoid overlap with that of the W3 channel. As demonstrated, high thermal inertia values fit the data at low heliocentric distance whilst low thermal inertia values fit the data at high heliocentric distance.
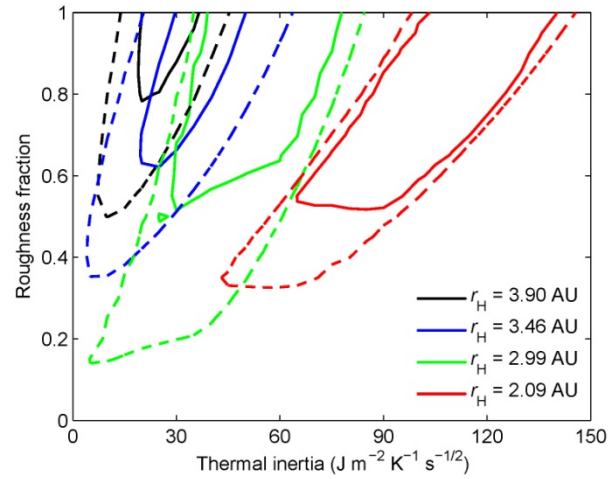
Figure 3: Results of chi-square fitting to the four different datasets of (1036) Ganymed when assuming a 4.6 μm spectral emissivity of 0.9. The solid and dashed contours indicate the delta-chi-squared cut-off boundaries for 1-σ and 3-σ confidence levels, respectively. As shown, low thermal inertia values provide the best fits at high heliocentric distances, and high thermal inertia values provide the best fits at low heliocentric distances. Therefore, it was not possible to find a single thermal inertia value that fitted all of the data adequately.
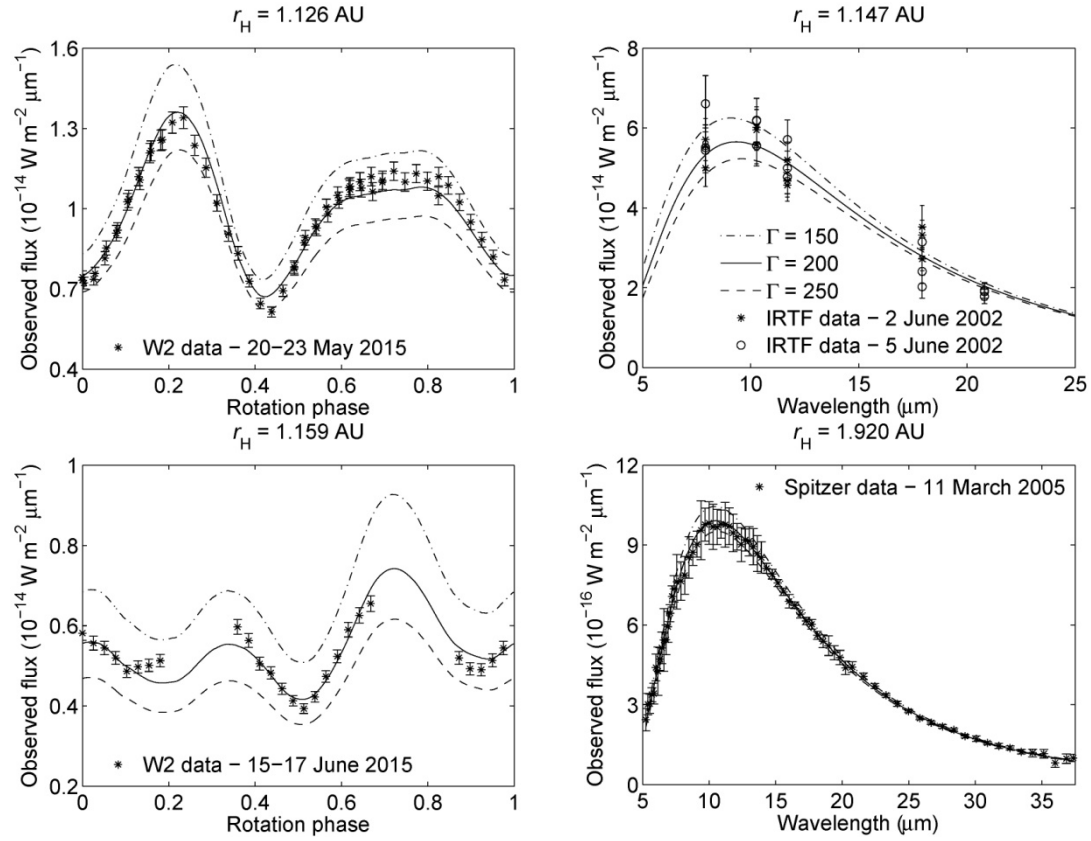
Figure 4: Thermal-infrared fits to the four different datasets of (1580) Betulia. The left panels give the fluxes measured by the reactivated NEOWISE mission in the W2 channel, the top right panel gives the fluxes measured by the NASA IRTF telescope, and the bottom right panel gives the fluxes measured by the Spitzer space telescope. The error bars represent the 1-σ uncertainties on the measured flux data points. The lines represent the ATPM fits to each dataset where the different line styles correspond to the different thermal inertia values indicated in the legend of the top right panel. For the NASA IRTF data, the data points have been light-curve scaled to a common rotation phase, i.e. corresponding to that of the first measurement of the 5 June 2002 subset of observations, in order to allow direct comparison of the observed fluxes as a function of wavelength. For the Spitzer data, only one in every five data points is plotted to ensure clarity of the figure. As demonstrated, a similar thermal inertia value fits each dataset equally well.
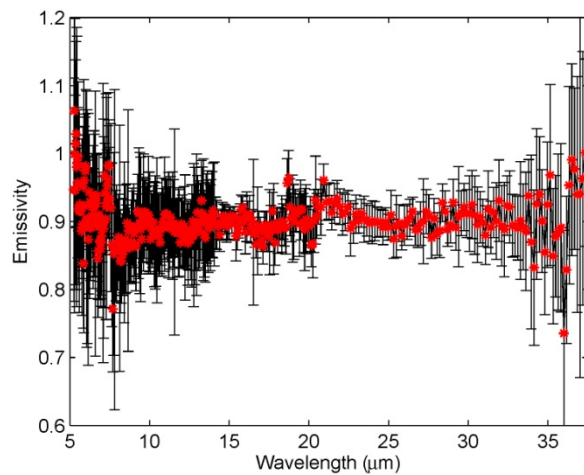
Figure 5: Emissivity spectrum of (1580) Betulia as obtained from Spitzer space telescope observations. The error bars represent the 1-σ uncertainties on the derived emissivity values.
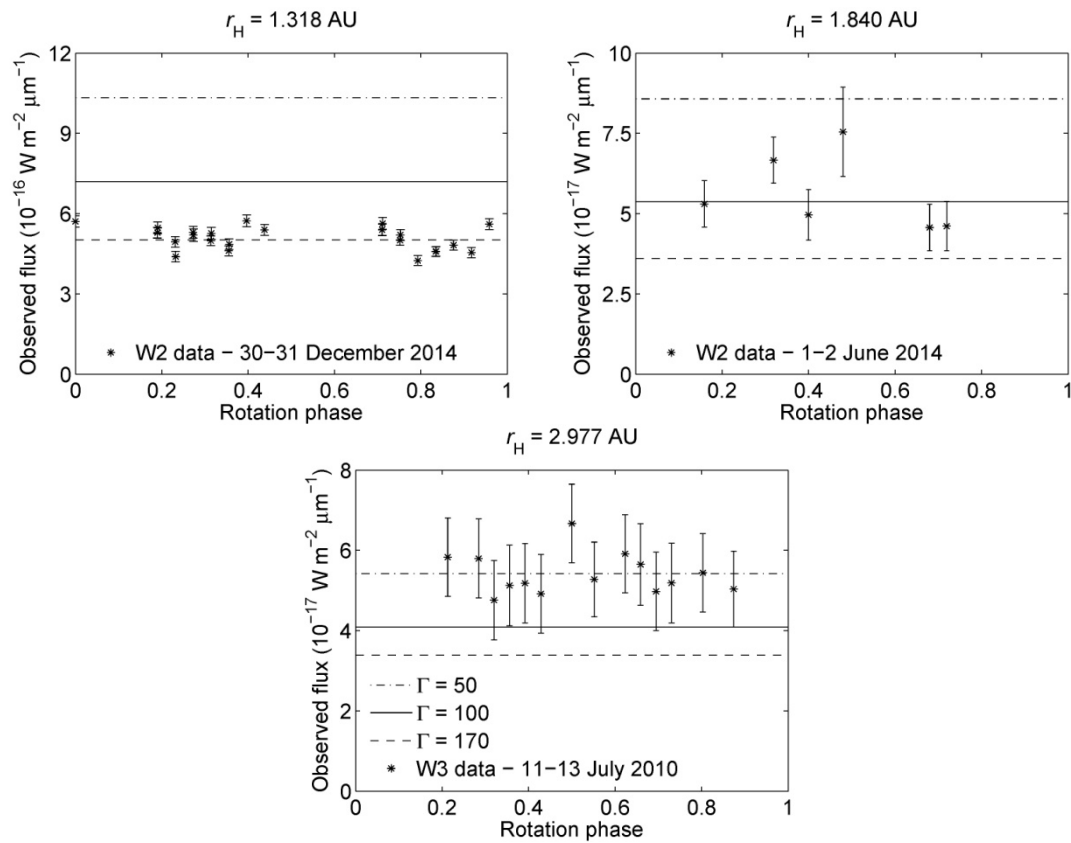
Figure 6: Thermal-infrared fits to the three different datasets of (276049) 2002 CE26. The top two panels give the fluxes measured by the reactivated NEOWISE mission in the W2 channel, and the bottom panel gives the fluxes measured by the main NEOWISE mission in the W3 channel. The error bars represent the 1-σ uncertainties on the measured flux data points. The lines represent the ATPM fits to each dataset where the different line styles correspond to the different thermal inertia values indicated in the legend of the bottom panel. As demonstrated, a high thermal inertia value fits the data at low heliocentric distance whilst a low thermal inertia value fits the data at high heliocentric distance.
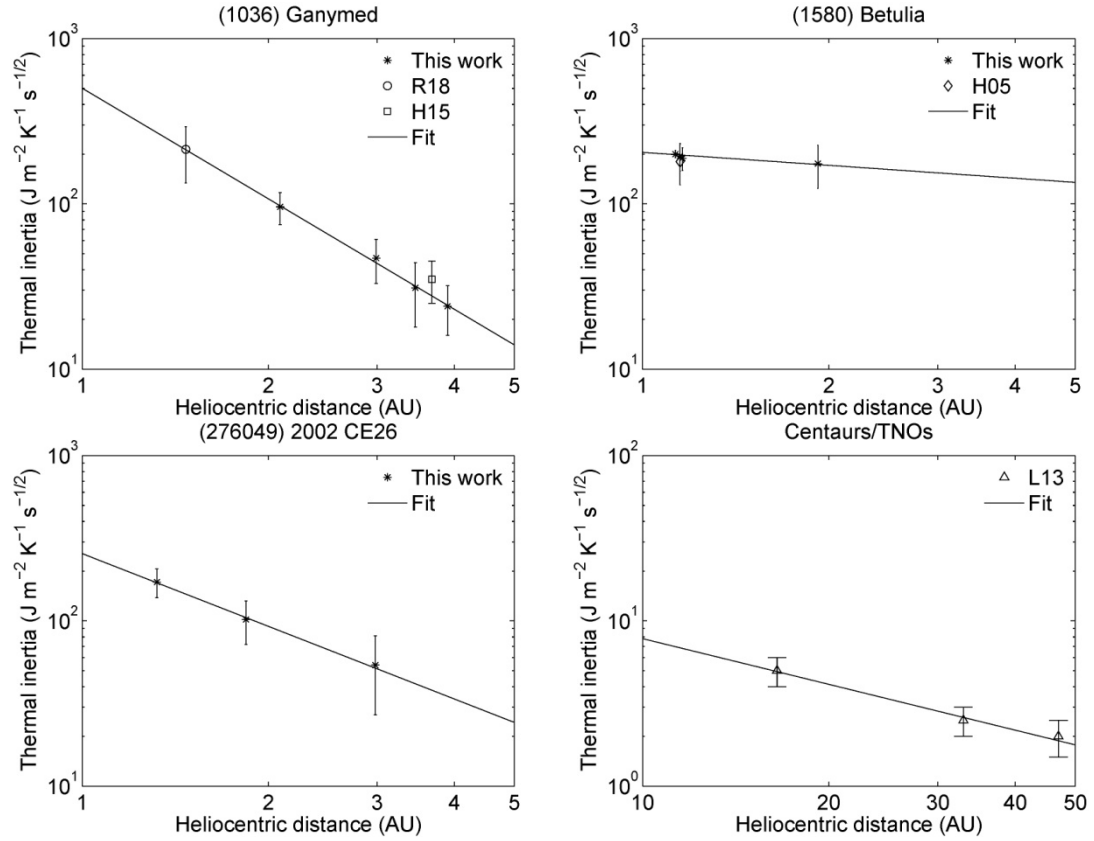
Figure 7: Asteroid thermal inertia as a function of heliocentric distance when assuming a 4.6 µm spectral emissivity of 0.9. The data points represent the thermal inertia measurements of each asteroid obtained by thermophysical modelling, and the error bars represent the 1-σ uncertainties on the measured thermal inertia values. The lines represent the best fit of equation (3) to the thermal inertia values as a function of heliocentric distance. The markers R18, H15, H05, and L13 refer to thermal inertia measurements obtained by Rivkin et al. (2018), Hanus et al. (2015), Harris et al. (2005), and Lellouch et al. (2013), respectively.
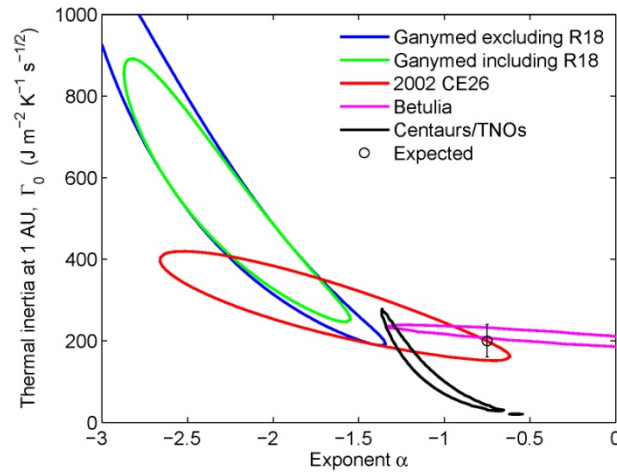
Figure 8: Results of chi-square fitting to determine the thermal inertia at 1 AU, Γ_0, and the exponent α for (1036) Ganymed, (1580) Betulia, (276049) 2002 CE26, and Centaurs/TNOs. This was performed by fitting equation (3) to the thermal inertia versus heliocentric distance trends displayed in Figure 7. The contours represent the 1-σ confidence level boundaries on the derived parameters for the objects considered. The data point represents what was previously expected for a typical km-sized near-Earth asteroid, i.e. a thermal inertia at 1 AU of 200 ± 40 J m^{-2} K^{-1} s$^{-1/2}$ with an exponent α of -0.75 (Delbo et al. 2007). R18 refers to the thermal inertia measurement of Ganymed obtained by Rivkin et al. (2018).
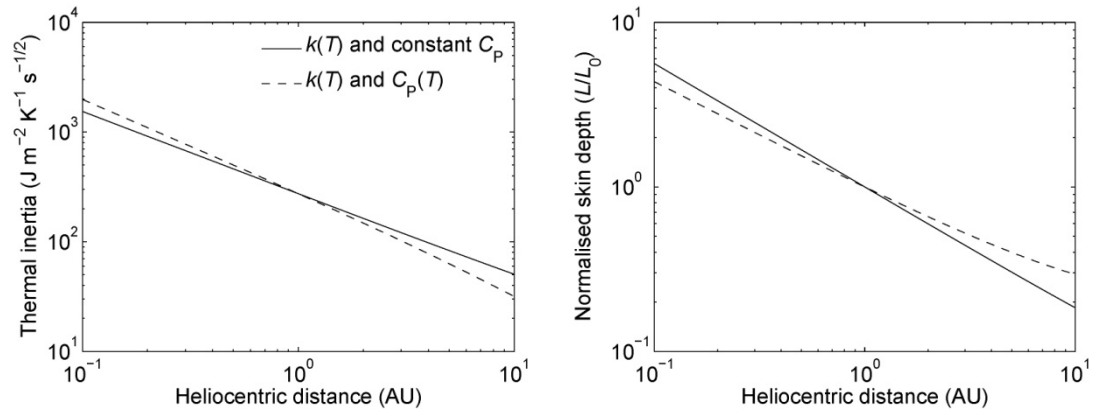
Figure 9: Theoretical predictions of the variation of asteroid thermal inertia (left panel) and thermal skin depth (right panel) with heliocentric distance. As indicated, these predictions either included just the temperature-dependence of thermal conductivity (solid lines), or they included the temperature-dependence of both the thermal conductivity and the specific heat capacity (dashed lines). The thermal conductivity and specific heat capacity were calculated using equations (4) and (7), respectively, for the example asteroid discussed in Section 3.1. The associated thermal skin depth was calculated using equation (8), and has been normalised by taking its ratio to the thermal skin depth at 1 AU, L_0.
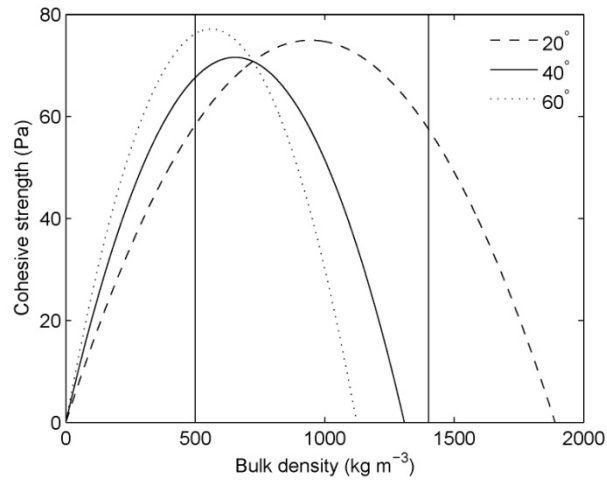
Figure 10: Minimum cohesive strength of (276049) 2002 CE26. The calculation used the Drucker-Prager failure criterion (Holsapple 2007) as a function of the bulk density (*x* axis) and angle of friction (legend) for the dynamically equivalent and equal volume ellipsoid of 2002 CE26, i.e. the ellipsoid has semi-axes of a = 1.80, b = 1.79, and c = 1.61 km. The vertical lines represent the 1-σ range determined for the bulk density of 2002 CE26, i.e. 900 $^{+500}/_{-400}$ kg m^{-3} (Shepard et al. 2006).
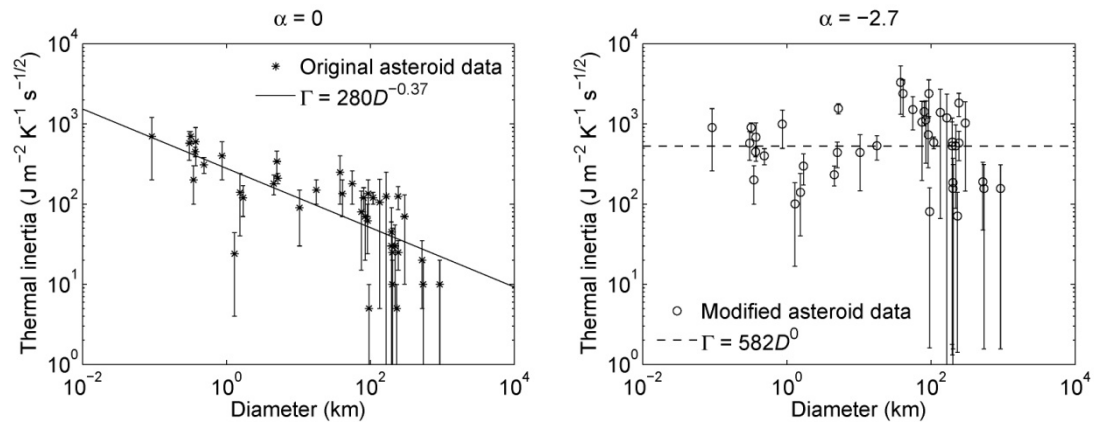
Figure 11: Asteroid thermal inertia as a function of size. The 40 asteroids shown here consists of 14 near-Earth asteroids and 26 main-belt asteroids. The original data shown in the left panel was obtained from Table 2 of Delbo et al. (2015) and has no adjustment for heliocentric distance. As shown, there is an obvious trend of decreasing asteroid thermal inertia with increasing size. The modified data shown in the right panel uses the same set of asteroids but their thermal inertia values have now been adjusted for heliocentric distance using equation (3) with an exponent α of -2.7. As shown in this case, there is no longer a trend of decreasing asteroid thermal inertia with increasing size.
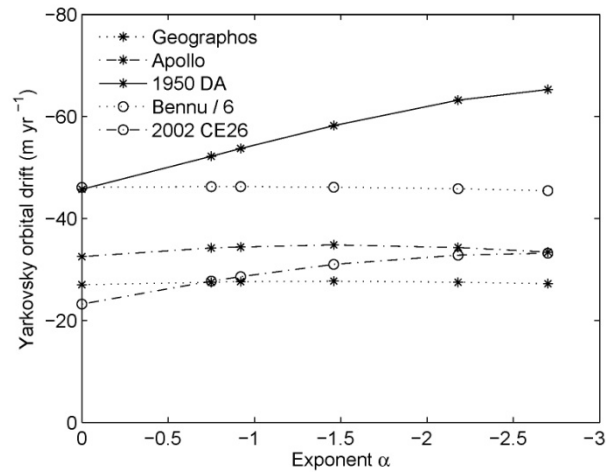
Figure 12: The influence of the heliocentric distance variation exponent α on the Yarkovsky orbital drift of five near-Earth asteroids. For these calculations, the asteroids were assumed to have a surface roughness fraction of 0.5 and a thermal inertia value of 340 J m^{-2} K^{-1} s$^{-1/2}$ at 1.1 AU for (1620) Geographos, 140 J m^{-2} K^{-1} s$^{-1/2}$ at 1.0 AU for (1862) Apollo, 24 J m^{-2} K^{-1} s$^{-1/2}$ at 1.7 AU for (29075) 1950 DA, 310 J m^{-2} K^{-1} s$^{-1/2}$ at 1.1 AU for (101955) Bennu, and 100 J m^{-2} K^{-1} s$^{-1/2}$ at 1.8 AU for (276049) 2002 CE26. The Yarkovsky orbital drift of Bennu has been divided by a factor of 6 so that it can be plotted on the same scale as that used for the other four asteroids.

Tables

Table 1: Summary of physical properties for the three near-Earth asteroids studied.

Asteroid	(1036) Ganymed[a]	(1580) Betulia[b]	(270649) 2002 CE26[c]
Size (km)	36 ± 1	5.39 ± 0.54	3.5 ± 0.4
Absolute magnitude	9.47	14.8	15.8
Phase parameter	0.31	0.15	-0.25
Geometric albedo	0.23 ± 0.01	0.07 ± 0.01	0.07 ± 0.02
Spectral type	S	C	C
Rotation period (hr)	10.31284	6.13836	3.2931
Pole orientation (°)	$\lambda_H = 190, \beta_H = -78$	$\lambda_H = 136, \beta_H = 22$	$\lambda_H = 317, \beta_H = -20$
Semimajor axis (AU)	2.66	2.20	2.23
Eccentricity	0.53	0.49	0.56

References: (a) Hanus et al. (2015); (b) Magri et al. (2007); (c) Shepard et al. (2006).

Table 2: Observation geometry and number of data points for the three near-Earth asteroids studied.

Asteroid	Observation date (UT)	Telescope	Heliocentric distance (AU)	Observer-centric distance (AU)	Phase angle (°)	Sub-solar latitude (°)	Sub-observer latitude (°)	Number of data points
(1036) Ganymed	15-16 January 2010	NEOWISE	3.896	3.722	14.6	-25.2	-25.5	12x W3 12x W4
	22-23 June 2010	NEOWISE	3.462	3.244	17.0	-18.3	-19.0	14x W3 14x W4
	14-15 February 2015	Reactivated NEOWISE	2.989	2.800	19.3	-11.0	-8.7	12x W2
	19-20 July 2015	Reactivated NEOWISE	2.093	1.684	28.7	7.1	6.7	15x W2
(1580) Betulia	02 June 2002 05 June 2002	NASA IRTF	1.143 1.150 (1.147)	0.246 0.264 (0.255)	52.9 53.3 (53.1)	12.7 15.2 (14.0)	-39.0 -33.6 (-36.3)	6x 7.91 µm 6x 10.27 µm 6x 11.70 µm 6x 17.93 µm 3x 20.81 µm
	11 March 2005	Spitzer	1.920	1.757	31.2	-56.7	-25.5	359x wavelengths at 5-38 µm
	20-23 May 2015	Reactivated NEOWISE	1.126	0.408	63.5	-4.5	-52.0	59x W2
	15-17 June 2015	Reactivated NEOWISE	1.159	0.422	60.0	18.1	-34.3	26x W2
(276049) 2002 CE26	11-13 July 2010	NEOWISE	2.977	2.734	19.9	9.2	29.0	14x W3
	1-2 June 2014	Reactivated NEOWISE	1.840	1.505	33.4	-26.8	-17.0	6x W2
	30-31 December 2014	Reactivated NEOWISE	1.318	0.874	48.2	26.9	-7.9	23x W2

Table 3: The influence of the spectral emissivity at 4.6 μm on the thermal inertia fitting results for (1036) Ganymed.

4.6 μm spectral emissivity	February 2015 observations (r_H = 2.99 AU)			July 2015 observations (r_H = 2.09 AU)			Combined reduced-χ^2	Simultaneous fit reduced-χ^2
	Thermal inertia (J m^{-2} K^{-1} s$^{-1/2}$)	Roughness fraction	Reduced-χ^2	Thermal inertia (J m^{-2} K^{-1} s$^{-1/2}$)	Roughness fraction	Reduced-χ^2		
0.6	33 ± 15	0.62 ± 0.25	0.38	50 ± 17	0.72 ± 0.19	0.68	0.53	1.58
0.7	38 ± 14	0.63 ± 0.24	0.45	66 ± 19	0.72 ± 0.19	0.67	0.54	2.56
0.8	42 ± 14	0.65 ± 0.24	0.52	82 ± 20	0.71 ± 0.19	0.67	0.55	3.47
0.9	47 ± 14	0.66 ± 0.23	0.59	96 ± 21	0.71 ± 0.19	0.67	0.56	4.61
1.0	50 ± 14	0.68 ± 0.22	0.64	110 ± 22	0.71 ± 0.19	0.67	0.57	6.71

For comparison purposes, the January (r_H = 3.90 AU) and June (r_H = 3.46 AU) 2010 observations of Ganymed gave thermal inertia values of 24 ± 8 and 31 ± 13 J m^{-2} K^{-1} s$^{-1/2}$ with reduced-χ^2 values of 0.68 and 0.39, respectively. The combined reduced-χ^2 value was calculated by combining the χ^2 values of the best individual fits from the four datasets using ten free parameters in total. The simultaneous fit reduced-χ^2 value was calculated by fitting all four datasets simultaneous using three free parameters.

Table 4: Thermal inertia fitting results for the three near-Earth asteroids studied when assuming a spectral emissivity at 4.6 μm of 0.9.

Asteroid	Heliocentric distance (AU)	Thermal inertia (J m^{-2} K^{-1} s$^{-1/2}$)	Roughness fraction	Source
(1036) Ganymed	1.240-1.970 (1.474)	214 ± 80	Not given	Rivkin et al. (2018)
	2.093	96 ± 21	0.71 ± 0.19	This work
	2.989	47 ± 14	0.66 ± 0.23	This work
	3.462	31 ± 13	0.77 ± 0.16	This work
	3.462 & 3.896 (3.679)	35 $^{+10}/_{-5}$	Not given	Hanus et al. (2015)
	3.896	24 ± 8	0.83 ± 0.13	This work
(1580) Betulia	1.126	200 ± 10	0.79 ± 0.05	This work
	1.147	180 ± 50	Not given	Harris et al. (2005)
		167 ± 54 (light-curve)	0.75 ± 0.19	This work
		195 ± 37 (radar)	0.67 ± 0.24	This work
	1.159	189 ± 30	0.78 ± 0.08	This work
	1.920	175 ± 51	0.76 ± 0.18	This work
(276049) 2002 CE26	1.318	172 ± 34	0.48 ± 0.30	This work
	1.840	102 ± 30	0.52 ± 0.30	This work
	2.977	54 ± 27	0.54 ± 0.30	This work

Table 5: The influence of the heliocentric distance variation exponent α on the asteroid thermal inertia versus size trend parameters d_0 and ξ.

Exponent α	1 km thermal inertia d_0 (J m^{-2} K^{-1} s$^{-1/2}$)	Exponent ξ
0	280 ± 62	-0.37 ± 0.05
-0.75	334 ± 74	-0.27 ± 0.05
-0.92	348 ± 78	-0.25 ± 0.05
-1.46	395 ± 89	-0.17 ± 0.06
-2.22	472 ± 111	-0.07 ± 0.06
-2.7	528 ± 129	0.00 ± 0.06

Table 6: The influence of the heliocentric distance variation exponent α on the Yarkovsky effect for five near-Earth asteroids.

Asteroid	Semimajor axis (AU)	Eccentricity	Thermal inertia (J m^{-2} K^{-1} s$^{-1/2}$)	Heliocentric distance measured (AU)	Exponent α					
					0	-0.75	-0.92	-1.46	-2.18	-2.7
					Yarkovsky orbital drift (m yr^{-1})					
(1620) Geographos	1.25	0.34	340 $^{+140}/_{-100}$	1.1	-27.0	-27.5	-27.6	-27.7	-27.5	-27.2
(1862) Apollo	1.47	0.56	140 $^{+140}/_{-100}$	1.0	-32.5	-34.2	-34.4	-34.8	-34.3	-33.4
(29075) 1950 DA	1.70	0.51	24 $^{+20}/_{-14}$	1.7	-45.7	-52.2	-53.7	-58.2	-63.2	-65.3
(101955) Bennu	1.13	0.20	310 ± 70	1.1	-276.6	-277.4	-277.4	-276.8	-274.9	-272.7
(276049) 2002 CE26	2.23	0.56	100 ± 30	1.8	-23.2	-27.7	-28.6	-31.0	-32.8	-33.2

ONLINE SUPPLEMENTARY MATERIAL

Observing the variation of asteroid thermal inertia with heliocentric distance
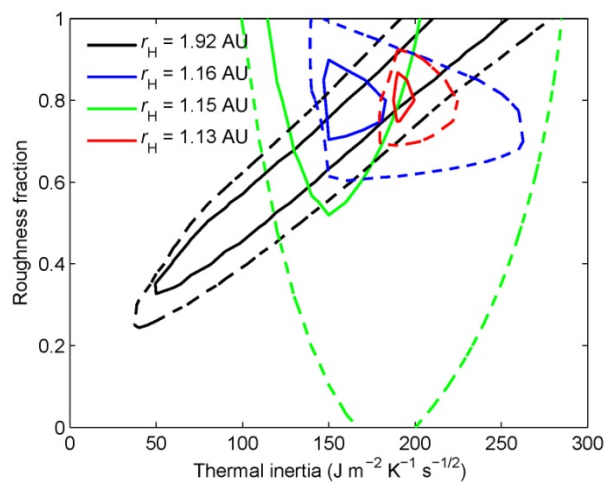B. Rozitis, S. F. Green, E. MacLennan & J. P. Emery

No. of Supplementary Material Pages: 10
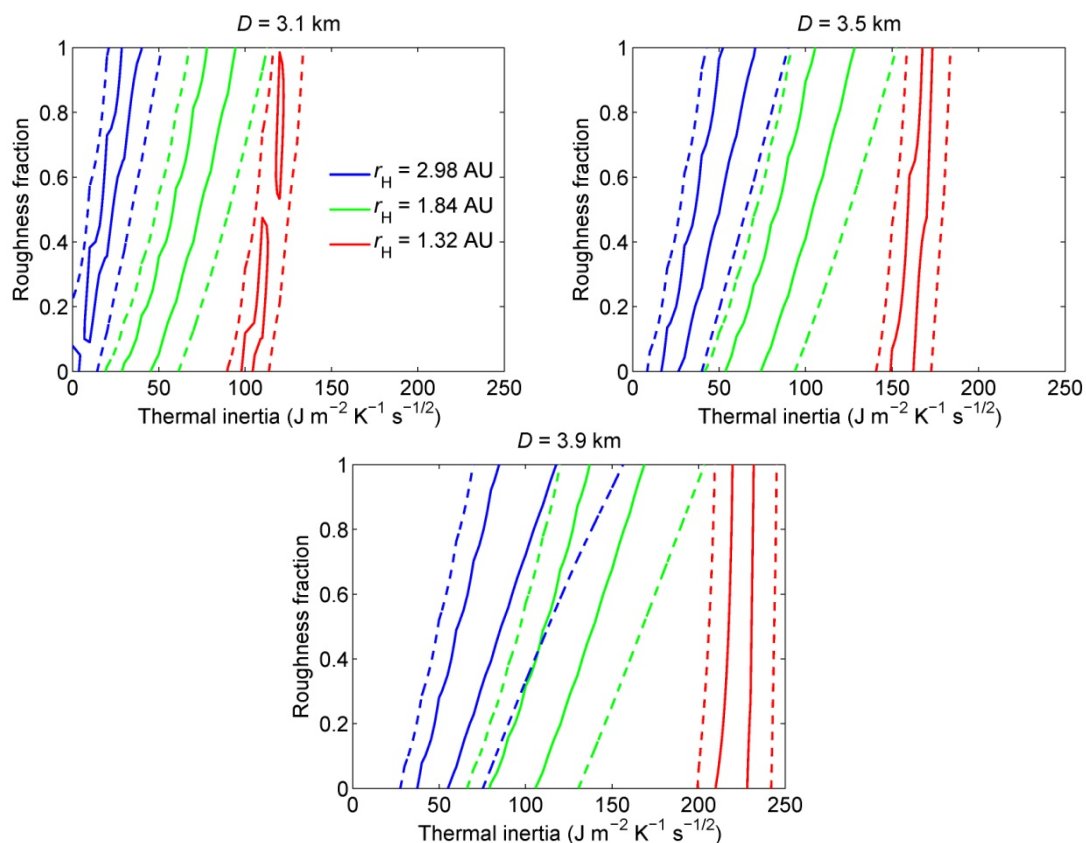No. of Supplementary Figures: 4
No. of Supplementary Tables: 5

Email correspondence: benjamin.rozitis@open.ac.uk

Supplementary figures



Supplementary Figure S1: Results of chi-square fitting to the four different datasets of (1580) Betulia when assuming a 4.6 μm spectral emissivity of 0.9. The solid and dashed contours indicate the delta-chi-squared cut-off boundaries for 1-σ and 3-σ confidence levels, respectively. As shown, similar thermal inertia and surface roughness values are obtained for each dataset.

Supplementary Figure S2: Results of chi-square fitting to the three different datasets of (276049) 2002 CE26 when assuming a 4.6 µm spectral emissivity of 0.9. The solid and dashed contours indicate the delta-chi-squared cut-off boundaries for 1-σ and 3-σ confidence levels, respectively. The delta-chi-squared contours have been resolved by diameter to demonstrate that little overlap exists between the three different datasets at identical diameter values. As shown, low thermal inertia values provide the best fits at high heliocentric distances, and high thermal inertia values provide the best fits at low heliocentric distances. Therefore, it was not possible to find a single thermal inertia value that fitted all of the data adequately.
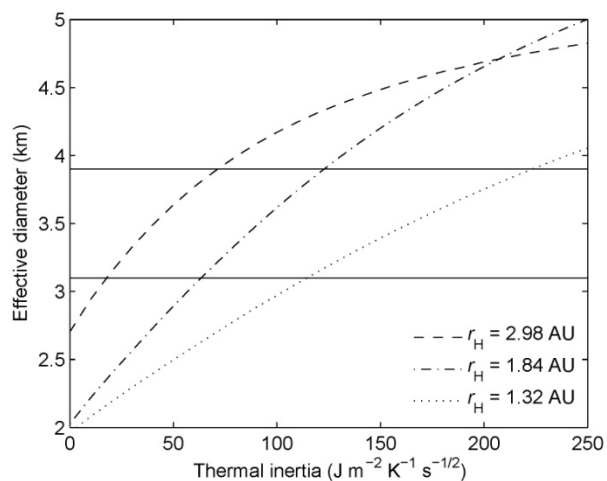
Supplementary Figure S3: Fitted effective diameter of (276049) 2002 CE26 as a function of thermal inertia for its three different datasets. The horizontal lines represent the radar diameter constraint of 3.5 ± 0.4 km from Shepard et al. (2006). Acceptable thermal inertia values are those which produce effective diameters that fall within the radar diameter constraint.
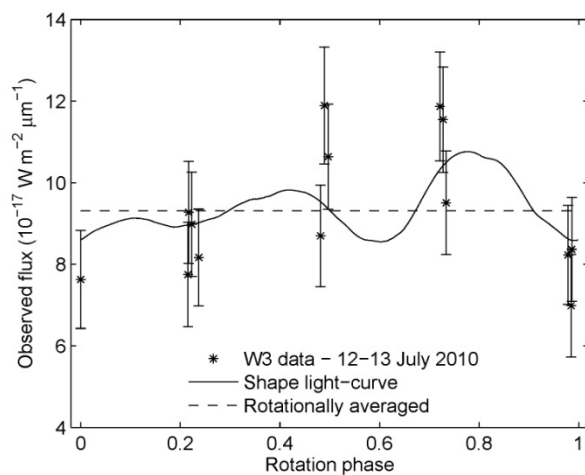
Supplementary Figure S4: Thermal-infrared fits to the NEOWISE observations of (29075) 1950 DA (modified from Rozitis et al. 2014). The solid line represents the fit previously obtained in Rozitis et al. (2014) using a thermal inertia of 24 J m^{-2} K^{-1} s$^{-1/2}$. The dashed line represents the fit obtained by rotationally averaging the model flux using a thermal inertia of 26 J m^{-2} K^{-1} s$^{-1/2}$. The error bars represent the 1-σ uncertainties on the measured flux data points.

Supplementary tables

Supplementary Table S1: Comparison of results between the standard analysis methodology and the alternative bootstrap analysis methodology for (1036) Ganymed.

4.6 μm spectral emissivity	February 2015 observations (r_H = 2.99 AU)		July 2015 observations (r_H = 2.09 AU)	
	Standard analysis thermal inertia (J m^{-2} K^{-1} s$^{-1/2}$)	Bootstrap analysis thermal inertia (J m^{-2} K^{-1} s$^{-1/2}$)	Standard analysis thermal inertia (J m^{-2} K^{-1} s$^{-1/2}$)	Bootstrap analysis thermal inertia (J m^{-2} K^{-1} s$^{-1/2}$)
0.6	33 ± 15	40 ± 13	50 ± 17	55 ± 17
0.7	38 ± 14	45 ± 13	66 ± 19	71 ± 18
0.8	42 ± 14	50 ± 13	82 ± 20	85 ± 20
0.9	47 ± 14	55 ± 13	96 ± 21	98 ± 21
1.0	50 ± 14	58 ± 13	110 ± 22	111 ± 23

For comparison purposes, the January (r_H = 3.90 AU) and June (r_H = 3.46 AU) 2010 observations of Ganymed gave thermal inertia values of 24 ± 8 and 31 ± 13 J m^{-2} K^{-1} s$^{-1/2}$ when using the standard methodology, and gave thermal inertia values of 27 ± 6 and 34 ± 9 J m^{-2} K^{-1} s$^{-1/2}$ when using the bootstrap methodology, respectively.

Supplementary Table S2: The influence of the spectral emissivity at 4.6 µm on the thermal inertia fitting results for (1580) Betulia.

4.6 µm spectral emissivity	May 2015 observations (r_H = 1.13 AU)			June 2015 observations (r_H = 1.16 AU)		
	Thermal inertia (J m^{-2} K^{-1} s$^{-1/2}$)	Roughness fraction	Reduced-χ^2	Thermal inertia (J m^{-2} K^{-1} s$^{-1/2}$)	Roughness fraction	Reduced-χ^2
0.6	79 ± 22	0.92 ± 0.05	0.82	108 ± 23	0.83 ± 0.10	1.89
0.7	114 ± 16	0.88 ± 0.06	0.94	136 ± 26	0.81 ± 0.09	1.94
0.8	155 ± 12	0.84 ± 0.05	1.11	163 ± 28	0.80 ± 0.09	2.03
0.9	200 ± 10	0.79 ± 0.05	1.39	189 ± 30	0.78 ± 0.08	2.13
1.0	247 ± 9	0.75 ± 0.06	1.78	210 ± 28	0.77 ± 0.08	2.21

For comparison purposes, the June 2002 (r_H = 1.15 AU) and March 2005 (r_H = 1.92 AU) observations of Betulia gave thermal inertia values of 195 ± 37 and 175 ± 51 J m^{-2} K^{-1} s$^{-1/2}$ with reduced-χ^2 values of 1.09 and 0.25, respectively.

Supplementary Table S3: The influence of the spectral emissivity at 4.6 µm on the thermal inertia fitting results for (276049) 2002 CE26.

4.6 µm spectral emissivity	June 2014 observations (r_H = 1.84 AU)			December 2014 observations (r_H = 1.32 AU)			Combined reduced-χ^2	Simultaneous fit reduced-χ^2
	Thermal inertia (J m^{-2} K^{-1} s$^{-1/2}$)	Roughness fraction	Reduced-χ^2	Thermal inertia (J m^{-2} K^{-1} s$^{-1/2}$)	Roughness fraction	Reduced-χ^2		
0.6	54 ± 22	0.51 ± 0.30	1.97	91 ± 23	0.48 ± 0.30	1.06	0.91	1.43
0.7	70 ± 24	0.51 ± 0.30	1.96	117 ± 26	0.48 ± 0.30	1.06	0.91	1.63
0.8	86 ± 27	0.51 ± 0.30	1.96	144 ± 29	0.48 ± 0.30	1.05	0.91	1.80
0.9	102 ± 30	0.52 ± 0.30	1.96	172 ± 34	0.48 ± 0.30	1.05	0.91	1.94
1.0	118 ± 34	0.52 ± 0.30	1.96	201 ± 39	0.48 ± 0.30	1.05	0.91	2.07

For comparison purposes, the July 2010 (r_H = 2.98 AU) observations of 2002 CE26 gave a thermal inertia value of 54 ± 27 J m^{-2} K^{-1} s$^{-1/2}$ with a reduced-χ^2 value of 0.30. The combined reduced-χ^2 value was calculated by combining the χ^2 values of the best individual fits from the three datasets using six free parameters in total. The simultaneous fit reduced-χ^2 value was calculated by fitting all three datasets simultaneous using two free parameters.

Supplementary Table S4: The influence of the spectral emissivity at 4.6 μm on the parameters describing the variation of thermal inertia with heliocentric distance for (1036) Ganymed and (276049) 2002 CE26.

4.6 μm spectral emissivity	(1036) Ganymed		(276049) 2002 CE26	
	Thermal inertia at 1 AU Γ_0 (J m^{-2} K^{-1} s$^{-1/2}$)	Exponent α	Thermal inertia at 1 AU Γ_0 (J m^{-2} K^{-1} s$^{-1/2}$)	Exponent α
0.6	$215\,^{+335}/_{-150}$	$-1.66\,^{+1.04}/_{-1.06}$	$105\,^{+110}/_{-55}$	$-0.78\,^{+0.78}/_{-1.78}$
0.7	$325\,^{+380}/_{-200}$	-1.96 ± 0.88	$155\,^{+125}/_{-75}$	$-1.12\,^{+1.02}/_{-1.44}$
0.8	$430\,^{+390}/_{-245}$	$-2.14\,^{+0.76}/_{-0.74}$	$200\,^{+145}/_{-85}$	$-1.28\,^{+0.88}/_{-1.32}$
0.9	$500\,^{+400}/_{-255}$	$-2.22\,^{+0.68}/_{-0.66}$	$255\,^{+165}/_{-105}$	$-1.46\,^{+0.86}/_{-1.22}$
1.0	$575\,^{+405}/_{-280}$	$-2.30\,^{+0.64}/_{-0.60}$	$315\,^{+195}/_{-125}$	$-1.62\,^{+0.82}/_{-1.14}$

Supplementary Table S5: The reflectance properties of (1036) Ganymed determined from different assumptions of its spectral emissivity at 4.6 μm.

4.6 μm spectral emissivity	January 2010 reflectance ratio	June 2010 reflectance ratio	Combined reflectance ratio*	February 2015 thermal component (%)	July 2015 thermal component (%)
0.6	1.39 ± 0.14	1.40 ± 0.09	1.36 ± 0.11	36.5 ± 6.4	80.2 ± 2.0
0.7	1.35 ± 0.13	1.32 ± 0.08	1.32 ± 0.10	38.6 ± 5.8	80.9 ± 1.8
0.8	1.30 ± 0.13	1.24 ± 0.08	1.27 ± 0.10	40.7 ± 6.0	81.6 ± 1.8
0.9	1.26 ± 0.13	1.15 ± 0.08	1.23 ± 0.11	42.6 ± 6.2	82.2 ± 1.8
1.0	1.21 ± 0.13	1.07 ± 0.08	1.19 ± 0.13	44.7 ± 6.9	82.7 ± 2.1

*Combined with the reflectance ratio of 1.28 ± 0.05 determined from the near-infrared spectral observations of Rivkin et al. (2018).